Following the Higgs mode across the BCS-BEC crossover in two dimensions

Dan Phan and Andrey V. Chubukov

School of Physics and Astronomy, University of Minnesota, Minneapolis, Minnesota 55455, USA

Although substantial effort has been dedicated to analyzing the Higgs (amplitude) mode in superconducting systems, there are relatively few studies of the Higgs peak's dispersion and width, quantities which are observable in spectroscopic measurements. These properties can be obtained from the location of the pole of the amplitude (Higgs) susceptibility in the lower half plane of complex frequency. We analyze the behavior of the Higgs mode in a two-dimensional neutral fermionic superfluid at $T = 0$ throughout the crossover from Bardeen-Cooper-Schrieffer (BCS) to Bose-Einstein condensation (BEC) behavior. This occurs when the dressed chemical potential μ changes sign from positive to negative. For $\mu > 0$, we find a pole in the Higgs susceptibility in the lower half plane of frequency and demonstrate that it leads to a well-defined peak in spectroscopic probes. For $\mu < 0$, the pole still exists but is "hidden," not giving rise to a peak in spectroscopic probes. Extending this analysis to a charged superconductor, we find that the Higgs mode is unaffected by the long-range Coulomb interaction.

I. INTRODUCTION

Superconducting and superfluid phases of interacting fermions are characterized by spontaneous breaking of U(1) gauge symmetry, resulting in a nonzero complex order parameter $\Delta = |\Delta|e^{i\varphi}$. Fluctuations in this order parameter can be decomposed into fluctuations of the phase φ (the Anderson-Bogoliubov-Goldstone or ABG mode), and the amplitude $|\Delta|$ (the Higgs mode) [1–4]. The Higgs mode has traditionally been difficult to observe experimentally since, as a scalar field, it does not couple linearly to the electromagnetic field [5]. Indeed, until recently, the only clear experimental observation of the Higgs mode has been in $2H - \mathrm{NbSe_2}$ [6,7], due to the coexistence of charge-density wave order and superconductivity [3,8,9]. However, in the past decade, advances in ultrafast THz and Raman spectroscopy have led to numerous reports of observations of the Higgs mode in superconductors [10–19], cold-atom systems [20] and quantum magnets [21]. Recent proposals have also suggested that the Higgs mode could be observed in a superconductor biased with a dc supercurrent [22,23]. There have been numerous recent theoretical studies of the amplitude (Higgs) mode (see, e.g., Refs. [24–35]).

In a three-dimensional (3D) *s*-wave superconductor where the Fermi energy is much larger than the gap ($E_F \gg \Delta$), the Higgs mode has frequency $\omega_H = 2\Delta$ in the long-wavelength limit, $\mathbf{q} = 0$ [36]. As such, the Higgs mode lies on the edge of the two-particle continuum, where Cooper pairs break up into two Bogoliubov quasiparticles [37]. One consequence of this can be seen in the amplitude (Higgs) susceptibility describing amplitude oscillations, which exhibits a branch cut rather than a pole, $\chi_H(\omega + i\delta, \mathbf{q} = 0) \sim 1/(\omega^2 - 4\Delta^2)^{1/2}$ [33]. This square-root singularity leads to amplitude oscillations which decay in time as a power law [36], as opposed to the exponential decay one expects from a true pole.

At nonzero $\mathbf{q}$, the square-root singularity disappears, and the spectral function $\mathrm{Im}\chi_H(\omega + i\delta, \mathbf{q})$ develops a peak at a frequency ω above 2Δ, whose width is small but finite (see Fig. 1). It is natural to assume that a narrow peak at a frequency immediately above the real axis can be understood as resulting from a pole in $\chi_H(z, \mathbf{q})$ at a complex frequency $z_\mathbf{q} = \omega' + i\omega''$ slightly below the real axis. This is not guaranteed, however, because the presence of the two-particle continuum implies that the function $\chi_H(z, \mathbf{q})$ has branch cuts along the real-frequency axis for $|\omega| > 2\Delta$ [see Fig. 2(a)]. This branch cut implies that the behavior of $\chi_H(z, \mathbf{q})$ below the real axis [e.g., $\omega = \mathrm{Re}(z) > 2\Delta$] is not smoothly connected to the behavior of $\chi_H(\omega + i\delta, \mathbf{q})$. In contrast, $\chi_H(z, \mathbf{q})$ is smoothly connected to $\chi_H(\omega + i\delta, \mathbf{q})$ for $\omega < 2\Delta$ because there is no branch cut along the real axis in this case.

This line of reasoning suggests that more careful analysis is needed to determine whether the presence of a peak in $\mathrm{Im}\chi_H(\omega + i\delta, \mathbf{q})$ at $\omega > 2\Delta$ arises from a pole in $\chi_H(z, \mathbf{q})$ in the lower half plane and, conversely, whether the absence of such a peak implies that there is no pole in $\chi_H(z, \mathbf{q})$. To address this issue, one has to *analytically continue* $\chi_H(z, \mathbf{q})$ through the branch cut into the lower half plane and check whether this analytically continued susceptibility has a pole. We denote this function $\chi_H^\downarrow(z, \mathbf{q})$ below. It is equal to $\chi_H(z, \mathbf{q})$ in the upper half plane and is constructed to be smooth across the real-frequency axis for $|\omega| > 2\Delta$. The branch-cut structure of $\chi_H(z, \mathbf{q})$ and its analytical continuation $\chi_H^\downarrow(z, \mathbf{q})$ are illustrated in Figs. 2(a) and 2(b), respectively.

Since $\chi_H^\downarrow(z, \mathbf{q})$ is analytic across the real axis for $|\omega| > 2\Delta$, a pole in $\chi_H^\downarrow(z, \mathbf{q})$ at a frequency $z_\mathbf{q}$ close to the real axis, with $\mathrm{Re}(z_\mathbf{q}) > 2\Delta$, necessarily leads to a peak in $\mathrm{Im}\chi_H^\downarrow(z, \mathbf{q})$ immediately above the real axis. To highlight this, we have added in Fig. 2(b) vertical arrows from the positions of the poles (shown as crosses in the lower half plane) to $z = \omega + i\delta$. Henceforth, we refer to such poles as Higgs modes.

This reasoning does not hold for poles with $\mathrm{Re}(z_\mathbf{q}) < 2\Delta$, due to the *nonanalyticity* of $\chi_H^\downarrow(z, \mathbf{q})$ across the real axis for
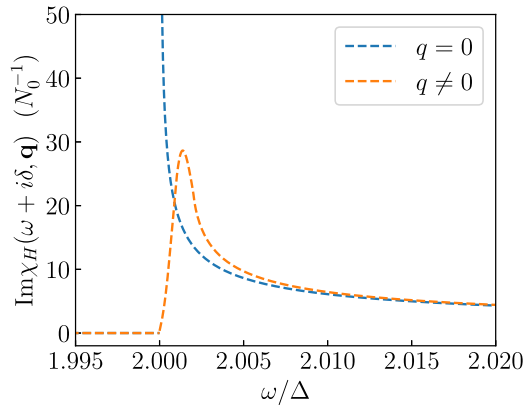
FIG. 1. Behavior of the Higgs susceptibility in the BCS regime, as a function of frequency at zero and nonzero q. The two-particle continuum begins at $\omega = 2\Delta$.
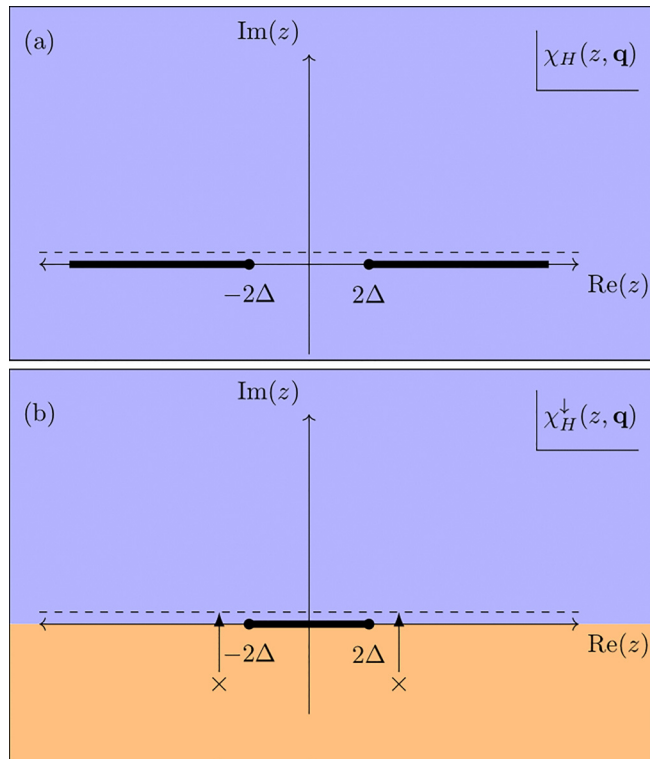

FIG. 2. The branch cut structure of (a) the Higgs susceptibility $\chi_H(z, \mathbf{q})$ and (b) its analytical continuation $\chi_H^{\downarrow}(z, \mathbf{q})$ in the complex z plane in the BCS regime, $\mu > 0$. In both panels, the dashed line indicates $z = \omega + i\delta$, the frequencies which are probed in spectroscopic experiments. The background coloring denotes Riemann sheets on which $\chi_H(z, \mathbf{q})$ and $\chi_H^{\downarrow}(z, \mathbf{q})$ are defined. The function $\chi_H(z, \mathbf{q})$ is defined on one Riemann sheet throughout the complex plane, while $\chi_H^{\downarrow}(z, \mathbf{q})$ is defined on two Riemann sheets, depending on the sign of $\text{Im}(z)$. Crosses in panel (b) show the position of poles in $\chi_H^{\downarrow}(z, \mathbf{q})$. Due to the analyticity of $\chi_H^{\downarrow}(z, \mathbf{q})$ across the real axis for $\omega > 2\Delta$, these poles lead to an experimentally observable peak in $\text{Im}\chi_H(\omega + i\delta, \mathbf{q})$. To highlight this, we added vertical arrows connecting these poles to the dashed line above the real axis. There are additional branch cuts in $\chi_H^{\downarrow}(z, \mathbf{q})$ at larger $|\omega|$, which we do not present here (see Sec. III). The presence of these additional branch cuts limits the frequency range where the poles of $\chi_H^{\downarrow}(z, \mathbf{q})$ give rise to peaks in $\text{Im}\chi_H(\omega + i\delta, \mathbf{q})$.

such $\text{Re}(z_\mathbf{q})$. In this case, there is no peak in $\text{Im}\chi_H(\omega + i\delta, \mathbf{q})$. The situation is similar to that of zero-sound collective modes in two dimensions (2D) for small, negative values of the Landau parameter F_0: the charge susceptibility has a pole in the lower half plane of frequency, but does not give rise to a peak in the spectral function due to a branch cut across the real axis [38]. Borrowing the notation from that paper, we refer to such a pole as a hidden mode.

From the perspective of complex analysis, it is natural to think of $\chi_H(z, \mathbf{q})$ and $\chi_H^{\downarrow}(z, \mathbf{q})$ as components of a single function defined on a Riemann surface, which consists of multiple Riemann sheets glued together along the real axis. From this perspective, the discontinuity in $\chi_H(z, \mathbf{q})$ across the real axis for $|\omega| > 2\Delta$ is a consequence of staying on the same Riemann sheet as we cross the real axis. Similarly, the smooth evolution of $\chi_H^{\downarrow}(\omega, \mathbf{q})$ across the real axis is obtained by transitioning from one Riemann sheet at $\text{Im}(z) > 0$ to another at $\text{Im}(z) < 0$.[1] We illustrate this in Fig. 2 via the background coloring: different coloring in Fig. 2(b) indicates that $\chi_H^{\downarrow}(z, \mathbf{q})$ lives on different Riemann sheets in the upper and lower half planes.

In this respect, the pole in $\chi_H^{\downarrow}(z, \mathbf{q})$ exists on an unphysical Riemann sheet, different from the physical Riemann sheet where $\text{Im}\chi_H^{\downarrow}(\omega + i\delta, \mathbf{q})$ is measured in spectroscopic probes [39,40]. However, due to the analyticity of $\chi_H^{\downarrow}(z, \mathbf{q})$ across the real axis for $\omega > 2\Delta$, poles on this unphysical Riemann sheet lead to observable peaks in the spectral function $\text{Im}\chi_H^{\downarrow}(\omega + i\delta, \mathbf{q})$. Such poles have been referred to as mirage modes in Ref. [38].

We re-iterate that a mirage mode with $|\omega| > 2\Delta$ on the unphysical Riemann sheet, if it exists, gives rise to a measurable peak in $\text{Im}\chi_H(\omega + i\delta, \mathbf{q})$. This is due to the analyticity of $\chi_H^{\downarrow}(z, \mathbf{q})$ for $|\omega| > 2\Delta$ along the vertical path connecting the pole at $z_\mathbf{q}$ in the lower half plane on an unphysical Riemann sheet, to the frequency $z = \text{Re}(z_\mathbf{q}) + i\delta$ in the upper half plane on the physical Riemann sheet.

On the other hand, if a pole of $\chi_H^{\downarrow}(z, \mathbf{q})$ on the unphysical Riemann sheet has $\text{Re}(z_\mathbf{q}) < 2\Delta$, it is no longer smoothly connected to the spectral function $\text{Im}\chi_H(\omega + i\delta, \mathbf{q})$ on the physical Riemann sheet. Instead, the pole at $z_\mathbf{q}$ leads to a peak in the spectral function evaluated on a different, unphysical Riemann sheet. The pole with $\text{Re}(z_\mathbf{q}) < 2\Delta$ then becomes a hidden mode.

In 3D, the analytic structure of $\chi_H^{\downarrow}(z, \mathbf{q})$ has been analyzed by Andrianov and Popov [41]. In the high-density BCS limit, where the chemical potential μ is much larger than the gap Δ, they found that a pole in $\chi_H^{\downarrow}(z, \mathbf{q})$ does exist, and its location is $z_\mathbf{q} = 2\Delta + (0.2369 - 0.2956i)(q^2/2m)(\mu/\Delta)$. We note that this result for $\text{Re}(z_\mathbf{q})$ disagrees with the commonly cited result for the Higgs mode dispersion, which in our notation reads $z_\mathbf{q} = 2\Delta + \frac{1}{3}(q^2/2m)(\mu/\Delta) - i\frac{\pi^2}{12}\sqrt{\mu/2m}q$ [3]. We discuss

---

[1]In fact, there are complications to this procedure. There is no way to construct a function which is analytic across the real axis for all $|\omega| > 2\Delta$. Here, one should think of $\chi_H^{\downarrow}(z, \mathbf{q})$ as being analytic for $|\omega| \in (2\Delta, \omega_2)$ for some frequency ω_2. We discuss the analytic continuation in more detail in Sec. III.

the reason for this disagreement in Sec. A of the Supplemental Material (SM) [42].

Away from the high-density limit, particle-hole symmetry disappears, leading to a coupling of the amplitude and phase fluctuations. Previous work [24,33] has suggested that this loss of particle-hole symmetry eventually leads to the disappearance of the Higgs mode. An analysis of this has been done recently by Kurkjian *et al.* [43]. Writing the dispersion of the Higgs mode as $z_{\mathbf{q}} = 2\Delta + \zeta(q^2/2m)(\mu/\Delta)$, they demonstrated that $\mathrm{Re}(\zeta)$ decreases from its high-density value of $\mathrm{Re}(\zeta) = 0.2369$ as one lowers the chemical potential μ, changes sign at $\mu_c \approx 0.8267\Delta$, and becomes negative for smaller μ. For $0 < \mu < \mu_c$, when the system approaches the BEC regime, the pole has $\mathrm{Re}(z_{\mathbf{q}}) < 2\Delta$. The authors then argued that this pole does not give rise to a peak in $\mathrm{Im}\chi_H(\omega + i\delta, \mathbf{q})$.

In this work, we extend the analysis by Kurkjian *et al.* to 2D, investigating the dispersion and damping rate of the Higgs mode in a neutral fermionic superfluid and a charged superconductor as a function of density at $T = 0$. In contrast to the 3D case where μ and Δ become comparable only at strong coupling, in 2D one can tune between the BCS and BEC regimes already at weak coupling by varying the fermionic density. This is because, for a parabolic dispersion in 2D, a two-fermion bound state exists even at arbitrarily weak attraction [44]. For values of E_F larger than E_0 (where E_0 is half the bound-state energy of two fermions in vacuum), the system is in the BCS regime ($\mu \gtrsim 0$). In the low-density limit where $E_F \ll E_0$, the system is instead in the BEC regime. Here, the chemical potential μ is strongly renormalized down from its normal-state value E_F and becomes negative, $\mu \approx -E_0$.

In the high-density BCS limit, we find a pole in $\chi_H^{\downarrow}(z, \mathbf{q})$ at $z_{\mathbf{q}} = 2\Delta + (0.5 - 0.4302i)(q^2/2m)(\mu/\Delta)$. As μ/Δ decreases, the pole moves to $z_{\mathbf{q}} = 2\Delta + (0.5 - i\beta)(q^2/2m)(\mu/\Delta)$, where β interpolates between 0.4302 at $\mu \gg \Delta$ and the much larger $\frac{e}{16}\sqrt{2\Delta/\mu}$ at $\mu \ll \Delta$. We also calculate the residue of the pole, finding that it scales linearly with q, as in 3D [43]. We next move away from the long-wavelength limit and trace the position of the pole in $\chi_H^{\downarrow}(z, \mathbf{q})$ as a function of q. We find that the Higgs mode quickly becomes heavily damped with increasing q.

Crossing from the BCS regime ($\mu > 0$) to the BEC regime ($\mu < 0$), we find that the Higgs mode becomes hidden for $\mu < \mu_c = 0$. We illustrate the situation in the BEC regime in Fig. 3, where the branch cut structure of $\chi_H(z, \mathbf{q})$ and $\chi_H^{\downarrow}(z, \mathbf{q})$ is presented in Figs. 3(a) and 3(b), respectively. Here, the branch points at $\pm 2\Delta$ have been replaced with $\pm\omega_{\min} \equiv \pm 2[\Delta^2 + (|\mu| + q^2/8m)^2]^{1/2}$, which is the lower bound of the two-particle continuum for $\mu < 0$. As in the case when $\mu > 0$, $\chi_H^{\downarrow}(z, \mathbf{q})$ has poles in the lower-half plane. However, we find that these poles are hidden below the branch cut in $\chi_H^{\downarrow}(z, \mathbf{q})$, extending from $-\omega_{\min}$ to $+\omega_{\min}$. Hence, as in 3D, the poles do not give rise to spectroscopic signatures at frequencies immediately above the real axis.

We then investigate how the dispersion and damping rate of the Higgs mode is modified by the inclusion of the long-range Coulomb interaction. Our calculations show that the dispersion, damping rate, and residue of the Higgs mode is
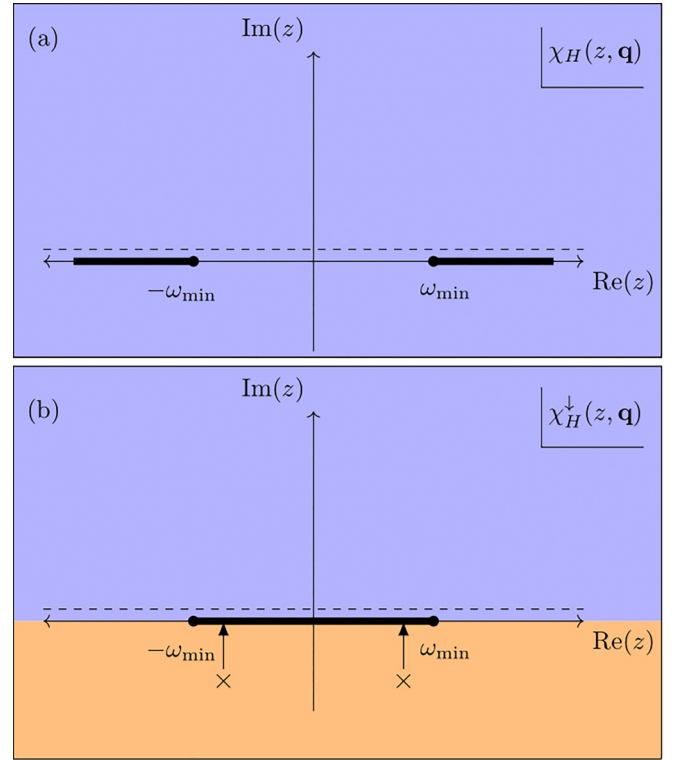

FIG. 3. The branch cut structure of (a) the Higgs susceptibility $\chi_H(z, \mathbf{q})$ and (b) its analytical continuation $\chi_H^{\downarrow}(z, \mathbf{q})$ in the complex z plane, in the BEC regime, where $\mu < 0$. In both panels, the dashed line indicates frequencies which are probed in spectroscopic experiments. The background color denotes Riemann sheets, and highlights that $\chi_H(z, \mathbf{q})$ in panel (a) is defined on one Riemann sheet throughout the complex plane. In contrast, $\chi_H^{\downarrow}(z, \mathbf{q})$ is defined on two Riemann sheets, depending on the sign of $\mathrm{Im}(z)$. The crosses in panel (b) indicate the position of the poles of $\chi_H^{\downarrow}(z, \mathbf{q})$. Unlike when $\mu > 0$, the poles lie below the threshold of the two-particle-continuum at $\omega_{\min} = 2[\Delta^2 + (|\mu| + q^2/8m)^2]^{1/2}$. The function $\chi_H^{\downarrow}(\omega, \mathbf{q})$ has a branch cut at $|\omega| < \omega_{\min}$, and the poles do not lead to observable peaks in $\mathrm{Im}\chi_H(\omega + i\delta, \mathbf{q})$. This is emphasized with the vertical arrows—the poles of $\chi_H^{\downarrow}(z, \mathbf{q})$ are obstructed from leading to a peak above the real axis due to the discontinuity across the branch cut.

unchanged from that of the neutral superfluid. We find that this is true in both two and three dimensions.

The paper is structured as follows: In Secs. II and III, we review how we obtain the Higgs susceptibility, using the functional-integral method within the Gaussian approximation. In Sec. IV, we then obtain the small-q dispersion, damping rate, and residue of the Higgs mode as a function of μ/Δ, neglecting the influence of the Coulomb interaction. In Sec. V, we extend this analysis and follow the dispersion of the Higgs mode as a function of $\mathbf{q}$, for arbitrary $\mathbf{q}$. In Sec. VI, we discuss the fate of the Higgs mode for $\mu < 0$. In Sec. VII, we repeat the analysis of the Higgs mode dispersion, including the effect of the Coulomb interaction. In Sec. VIII, we summarize our results.

II. MEAN-FIELD THEORY

To analyze the gap function and its fluctuations about equilibrium, we use the functional integral approach [45–47];

identical equations can also be obtained diagrammatically [48]. Assuming that fermions attract each other via a contact interaction $U(\mathbf{x} - \mathbf{y}) = -g\delta(\mathbf{x} - \mathbf{y})$ and neglecting for the moment the Coulomb interaction, the partition function is given by $Z = \int D(\bar{\psi}\psi) \exp(-S[\bar{\psi}, \psi])$, where the action $S[\bar{\psi}, \psi]$ in momentum space is given by

$$
\begin{aligned}
S[\bar{\psi}, \psi] = \sum_k \bar{\psi}_\sigma(k)\left(-i\omega_n + \frac{k^2}{2m} - \mu\right)\psi_\sigma(k) \\
- g\frac{T}{L^2} \sum_{kqp} \bar{\psi}_\uparrow(k + q/2)\bar{\psi}_\downarrow(-k + q/2) \\
\times \psi_\downarrow(-p + q/2)\psi_\uparrow(p + q/2).
\end{aligned} \tag{1}
$$

Here, L^2 denotes the area of our two-dimensional system, μ is the chemical potential, ψ_σ and $\bar{\psi}_\sigma$ are the Grassmann fields describing the fermionic degrees of freedom. The three-vectors k, p, and q label both Matsubara frequency and momentum, e.g., $k = (\omega_m, \mathbf{k})$. The Matsubara frequencies of k and p are fermionic [$\omega_m = (2m + 1)\pi T$], while the Matsubara frequency of q is bosonic ($\Omega_m = 2\pi mT$). To decouple the quartic interaction, we perform the Hubbard-Stratonovich transformation: we introduce the complex, bosonic field Δ_q, which couples to the $\bar{\psi}\bar{\psi}$ terms, and integrate out the fermionic fields ψ and $\bar{\psi}$. The partition function is then given by a functional integral over the complex field Δ_q, $Z = \int D(\Delta^*\Delta) \exp(-S_{\text{eff}}[\Delta^*, \Delta])$, where the effective action is

$$
S_{\text{eff}}[\Delta^*, \Delta] = \frac{\beta L^2}{g} \sum_q |\Delta_q|^2 - \text{Tr} \ln(-\beta \mathcal{G}^{-1}), \tag{2}
$$

and the Nambu-Gorkov Green's function in momentum-space is given by

$$
\mathcal{G}_{kp}^{-1} = \begin{pmatrix} (i\omega_n - \xi(\mathbf{k}))\delta_{kp} & \Delta_{k-p} \\ \Delta_{p-k}^* & (i\omega_n + \xi(\mathbf{k}))\delta_{kp} \end{pmatrix}. \tag{3}
$$

where $\xi(\mathbf{k}) = k^2/2m - \mu$, and μ is the chemical potential in a superconductor, which at this stage is a parameter.

Thus far, this procedure has been formally exact. To make further progress, we assume that the gap function at equilibrium is spatially uniform and frequency-independent, $\Delta_q = \Delta\delta_{q,0}$. This solution can be obtained by searching for a saddle point of the effective action. The condition $\delta S_{\text{eff}}/\delta\Delta = 0$ yields the conventional gap equation:

$$
\frac{1}{g} = \int \frac{d^2p}{(2\pi)^2} \frac{\tanh(\beta E_p/2)}{2E_p}. \tag{4}
$$

Here, $E_p = [\xi(\mathbf{p})^2 + |\Delta|^2]^{1/2}$. To handle the UV-divergence on the right-hand side, we impose a high-energy cutoff Λ, only considering momenta with $p^2/2m < \Lambda$.

The chemical potential μ is determined by the conservation of particle number. This constraint is enforced by using $n = -\partial\Omega/\partial\mu$, where Ω is the thermodynamic potential. Within the mean-field approximation, we have in equilibrium,

$\Omega = TS_{\text{eff}}[|\Delta|]$, and the equation enforcing particle-number conservation becomes

$$
n = \int \frac{d^2p}{(2\pi)^2} \left[1 - \frac{\xi(\mathbf{p})}{E_p} \tanh(\beta E_p/2)\right]. \tag{5}
$$

Due to the U(1) symmetry of the problem, we have the freedom to choose the phase of the order parameter. As such, we henceforth take Δ to be real.

At $T = 0$, Eqs. (4) and (5) can be solved for μ and Δ [44,49], and one finds

$$
\mu = E_F - E_0, \tag{6}
$$

$$
\Delta = 2\sqrt{E_F E_0}, \tag{7}
$$

where $E_0 = \Lambda e^{-2/N_0 g}$ is half the binding energy of two fermions in vacuum.

III. GAUSSIAN FLUCTUATIONS

To account for the effects of fluctuations in the order parameter, we expand the gap about the mean-field solution, $\Delta(x) = \Delta[1 + \lambda(x)]e^{i\theta(x)} \approx \Delta[1 + \lambda(x) + i\theta(x)]$, where $\lambda(x)$ and $\theta(x)$ are real dimensionless fields denoting the amplitude and phase fluctuations of the gap, respectively. By inserting this into the effective action and expanding about the saddle point, we find that S_{eff} is given to quadratic order by

$$
S_{\text{eff}} = S_0[\Delta] + \beta L^2 \Delta^2 \sum_q (\theta_q^* \quad \lambda_q^*)\hat{M}(i\Omega_m, \mathbf{q})\begin{pmatrix} \theta_q \\ \lambda_q \end{pmatrix}. \tag{8}
$$

The matrix $\hat{M}(i\Omega_m, \mathbf{q})$ is the inverse susceptibility for phase and amplitude fluctuations, and its matrix elements are given by

$$
M_{++}(z, \mathbf{q}) = \frac{1}{g} + \frac{1}{2}\chi_{22}(z, \mathbf{q}), \tag{9}
$$

$$
M_{--}(z, \mathbf{q}) = \frac{1}{g} + \frac{1}{2}\chi_{11}(z, \mathbf{q}), \tag{10}
$$

$$
M_{+-}(z, \mathbf{q}) = \frac{1}{2}\chi_{12}(z, \mathbf{q}), \tag{11}
$$

$$
M_{-+}(z, \mathbf{q}) = -M_{+-}(z, \mathbf{q}), \tag{12}
$$

where the plus and minus signs correspond to phase and amplitude fluctuations, respectively. The functions $\chi_{ij}(i\Omega_m, \mathbf{q})$ are defined as $\chi_{ij}(i\Omega_m, \mathbf{q}) = T/L^2 \sum_{\omega_m, \mathbf{p}} \text{Tr}[\mathcal{G}_{\text{MF}}(i\omega_m - i\Omega_m/2, \mathbf{p} - \mathbf{q}/2)\sigma_i \mathcal{G}_{\text{MF}}(i\omega_m + i\Omega_m/2, \mathbf{p} + \mathbf{q}/2)\sigma_j]$, where σ_i are the Pauli matrices, and $\mathcal{G}_{\text{MF}}$ is the mean-field Green's function. After performing the Matsubara summation over ω_m and analytically continuing $i\Omega_m \to z$ to complex frequencies in the upper half plane, we find at $T = 0$

$$
\chi_{11}(z, \mathbf{q}) = \int \frac{d^2p}{(2\pi)^2} \frac{E_+ + E_-}{E_+ E_-} \frac{\xi_+\xi_- + E_+E_- - \Delta^2}{z^2 - (E_+ + E_-)^2}, \tag{13}
$$

$$
\chi_{22}(z, \mathbf{q}) = \int \frac{d^2p}{(2\pi)^2} \frac{E_+ + E_-}{E_+ E_-} \frac{\xi_+\xi_- + E_+E_- + \Delta^2}{z^2 - (E_+ + E_-)^2}, \tag{14}
$$

$$
\chi_{12}(z, \mathbf{q}) = -iz \int \frac{d^2p}{(2\pi)^2} \frac{1}{E_+ E_-} \frac{\xi_+E_- + \xi_-E_+}{z^2 - (E_+ + E_-)^2}. \tag{15}
$$

Here, $\xi_{\pm} = (\mathbf{p} \pm \mathbf{q}/2)^2/(2m) - \mu$ and $E_{\pm} = (\xi_{\pm}^2 + \Delta^2)^{1/2}$. The Higgs susceptibility $\chi_H(z, \mathbf{q})$ is given within this Gaussian approximation by

$$\chi_H(z, \mathbf{q}) = \frac{M_{++}(z, \mathbf{q})}{\det \hat{M}(z, \mathbf{q})} \qquad (16)$$

and corresponds to a Fourier transform of the amplitude-amplitude correlation function $\chi_H(t, \mathbf{x}) = \langle \lambda(t, \mathbf{x})\lambda(0, 0) \rangle$. We note that, although we refer to the above expression the Higgs (amplitude) susceptibility, the above expression actually corresponds to the longitudinal susceptibility, which is in general not equal to the Higgs susceptibility [25]. However, because the longitudinal and Higgs susceptibility coincide within the Gaussian approximation, we will use these terms interchangeably.

In the high-density limit, one has particle-hole symmetry, so that the off-diagonal matrix elements $M_{+-} = M_{-+} = 0$. In this case, the phase and amplitude fluctuations are completely decoupled, and the Higgs susceptibility is simply given by $\chi_H(z, \mathbf{q}) \equiv \chi_{--}(z, \mathbf{q}) = 1/M_{--}(z, \mathbf{q})$. Away from the high-density limit, the amplitude-phase coupling is nonzero, and one should use Eq. (16). As discussed in the introduction, we search for the Higgs mode by calculating the location of the poles of $\chi_H^{\downarrow}(z, \mathbf{q})$, the analytical continuation of $\chi_H(z, \mathbf{q})$ into the lower half plane through the real axis at $\omega > 2\Delta$. We search for poles $z_{\mathbf{q}}$ of $\chi_H^{\downarrow}(\omega, \mathbf{q})$ by solving

$$\det \hat{M}^{\downarrow}(z_{\mathbf{q}}, \mathbf{q}) = 0. \qquad (17)$$

Analytical continuation procedure

We now outline how we analytically continue the matrix elements $M_{\sigma\sigma'}(z, \mathbf{q})$. In the introduction, we framed analytic continuation as stitching together functions evaluated on different Riemann sheets. Here, we discuss how this procedure is performed computationally.

To this end, recall that the purpose of analytic continuation is to obtain a function which is equal to $M_{\sigma\sigma'}(z, \mathbf{q})$ in the upper half plane, and analytic across the portion of the real axis where $\omega > 2\Delta$. For this purpose, we define the spectral densities

$$\rho_{\sigma\sigma'}(\omega, \mathbf{q}) = \frac{M_{\sigma\sigma'}(\omega + i\delta, \mathbf{q}) - M_{\sigma\sigma'}(\omega - i\delta, \mathbf{q})}{-2\pi i}. \qquad (18)$$

With this definition, we trivially have $M_{\sigma\sigma'}(\omega - i\delta, \mathbf{q}) - 2\pi i \rho_{\sigma\sigma'}(\omega, \mathbf{q}) = M_{\sigma\sigma'}(\omega + i\delta, \mathbf{q})$. If we view the expression $M_{\sigma\sigma'}(\omega - i\delta, \mathbf{q}) - 2\pi i \rho_{\sigma\sigma'}(\omega, \mathbf{q})$ as the value of a complex function $M_{\sigma\sigma'}^{\downarrow}(z, \mathbf{q})$ just below the real axis, then we have $M_{\sigma\sigma'}^{\downarrow}(\omega - i\delta, \mathbf{q}) = M_{\sigma\sigma'}(\omega + i\delta, \mathbf{q})$. Using this, the following function is by construction analytic across the real axis:

$$M_{\sigma\sigma'}^{\downarrow}(z, \mathbf{q}) = \begin{cases} M_{\sigma\sigma'}(z, \mathbf{q}) & \text{Im}(z) > 0 \\ M_{\sigma\sigma'}(z, \mathbf{q}) - 2\pi i \rho_{\sigma\sigma'}(z, \mathbf{q}) & \text{Im}(z) < 0. \end{cases} \qquad (19)$$

Note that, in this equation, we have replaced $\rho_{\sigma\sigma'}(\omega, \mathbf{q})$ with its analytical continuation away from the real axis,
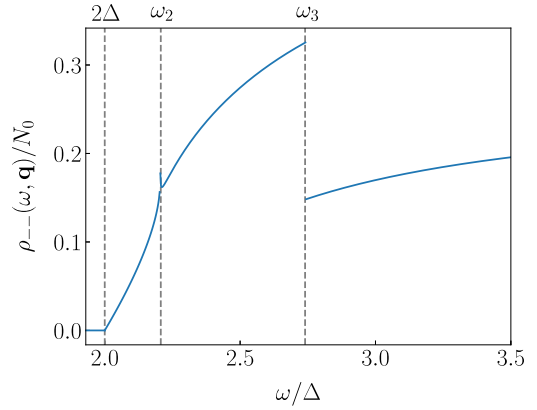

FIG. 4. The spectral density $\rho_{--}(\omega, \mathbf{q})$ at $\mu = \Delta$ and $q = 0.5\sqrt{2m\mu}$, as a function of ω. The frequencies ω_2 at which $\rho_{--}(\omega, \mathbf{q})$ has a kink, and ω_3, at which it is discontinuous, are defined in the text.

$\rho_{\sigma\sigma'}(z, \mathbf{q})$. This requires care, since $\rho_{\sigma\sigma'}(\omega, \mathbf{q})$ is not analytic for all $\omega > 2\Delta$—it has a kink at some higher frequency ω_2, and a discontinuity at even higher ω_3. We illustrate this in Fig. 4, where we plot $\rho_{--}(\omega, \mathbf{q})$ as a function of ω for $\mu = \Delta$ and $q = 0.5\sqrt{2m\mu}$. These kinks and discontinuities result from Lifshitz transitions, which we discuss in Sec. B of the SM [42]. To obtain a function which we can analytically continue away from the real axis, we must restrict the domain of $\rho_{--}(\omega, \mathbf{q})$ to a subset of the real axis on which $\rho_{--}(\omega, \mathbf{q})$ is analytic. Similar consideration holds for the other spectral densities $\rho_{\sigma\sigma'}(\omega, \mathbf{q})$.

Once we choose a region of the real axis on which $\rho_{\sigma\sigma'}(\omega, \mathbf{q})$ is analytic, we analytically continue $\rho_{\sigma\sigma'}(\omega, \mathbf{q})$ to obtain the complex function $\rho_{\sigma\sigma'}(z, \mathbf{q})$, and use Eq. (19) to obtain the analytic continuation of $M_{\sigma\sigma'}(z, \mathbf{q})$ into the lower half plane. The resulting $M_{\sigma\sigma'}^{\downarrow}(z, \mathbf{q})$ is analytic across the region of the real axis we have chosen.

Different choices of domains for $\rho_{\sigma\sigma'}(\omega, \mathbf{q})$ lead to distinct analytic behaviors in $M_{\sigma\sigma'}^{\downarrow}(z, \mathbf{q})$, and corresponds to defining $M_{\sigma\sigma'}^{\downarrow}(z, \mathbf{q})$ using different unphysical Riemann sheets in the lower half plane. Expressions for the spectral densities for arbitrary $\mathbf{q}$ and ω can be found in Sec. C of the SM [42], as well as their analytic continuations through the different regions of ω. For general values of $\mathbf{q}$, μ, and ω, the analytically continued matrix elements contain hyper-elliptic integrals, which we handle numerically. However, in some limits, expressions for the analytically continued matrix elements $M_{\sigma\sigma'}^{\downarrow}(z, \mathbf{q})$ turn out to be relatively simple (see the next section.)

Since we expect the Higgs mode to have frequencies just above the boundary of the two-particle continuum, we analytically continue $\rho_{\sigma\sigma'}(\omega, \mathbf{q})$ [and hence $M_{\sigma\sigma'}(\omega, \mathbf{q})$] through the region $(2\Delta, \omega_2)$ for $\mu > 0$. Doing so leads to matrix elements which are analytic across $(2\Delta, \omega_2)$, but discontinuous across other regions of the real axis. When $\mu < 0$, the lower bound of the two-particle continuum is instead at ω_3, which becomes the lower bound of the two-particle continuum $\omega_{\min}$, so we analytically continue the matrix elements through the region $(\omega_{\min}, \infty)$. This procedure leads to matrix elements which are analytic across $(\omega_{\min}, \infty)$, but discontinuous across, e.g., the region $(0, \omega_{\min})$.

IV. THE LONG-WAVELENGTH DISPERSION OF THE HIGGS MODE

In this section, we calculate the dispersion of the Higgs mode at small $\mathbf{q}$ and $\mu > 0$. As discussed in the previous section, this is done by first constructing $\chi_H^{\downarrow}(z, \mathbf{q})$, the analytical continuation of $\chi_H(z, \mathbf{q})$ into the lower half plane through $\omega \in (2\Delta, \omega_2)$. This region is chosen because we expect the Higgs mode to begin at $z_{\mathbf{q}=0} = 2\Delta$ and disperse quadratically with q to larger values of $\mathrm{Re}(z_{\mathbf{q}})$. We then search for a pole in $\chi_H^{\downarrow}(z, \mathbf{q})$ of the form $z_{\mathbf{q}} = 2\Delta + \zeta(q^2/2m)(\mu/\Delta)$. We see that $\omega_2 = 2\Delta + (q^2/2m)(\mu/\Delta)$ at small $\mathbf{q}$. Accordingly, we constrain $\mathrm{Re}(\zeta)$ to take values in the interval $(0,1)$—this ensures $\mathrm{Re}(z_{\mathbf{q}}) \in (2\Delta, \omega_2)$.

Below we compute the matrix elements $M_{\sigma\sigma'}(z, \mathbf{q})$ in the upper half plane and analytically continue them one by one through the real axis. We begin by calculating $M_{--}(z, \mathbf{q})$ using Eq. (11). Combining Eq. (14) with the gap equation

$\frac{1}{g} = \frac{1}{2} \int \frac{d^2 p}{(2\pi)^2} \frac{1}{E}$, we express $M_{--}(z, \mathbf{q})$ as

$$M_{--}(z, \mathbf{q}) = \frac{1}{4} \int \frac{d^2 p}{(2\pi)^2} \frac{E_+ + E_-}{E_+ E_-} \frac{z^2 - 4\Delta^2 - (\xi_+ - \xi_-)^2}{z^2 - (E_+ + E_-)^2}. \tag{20}$$

Evaluating this integral (the technical details can be found in Sec. A of the SM [42]), we obtain

$$M_{--}(z_{\mathbf{q}}, \mathbf{q}) = -iN_0 \frac{v_\mu q}{2\Delta} \sqrt{\zeta} E\left(\frac{1}{\sqrt{\zeta}}\right), \tag{21}$$

where $N_0 = m/2\pi$ is the density of states per spin in 2D, and $E(z)$ is the complete elliptic integral of the second kind.[2]

We now analytically continue $M_{--}(z_{\mathbf{q}}, \mathbf{q})$ into the lower half plane of complex z across $\omega \in (2\Delta, \omega_2)$, i.e., across $\zeta \in (0, 1)$. This is achieved by substituting $E(\frac{1}{\sqrt{\zeta}})$ at $\mathrm{Im}(\zeta) = 0^+$ by $E(\frac{1}{\sqrt{\zeta}}) + 2i\{E[(1 - \zeta^{-1})^{1/2}] - K[(1 - \zeta^{-1})^{1/2}]\}$ at $\mathrm{Im}(\zeta) = 0^-$ (see Sec. D of the SM for a proof [42]). The analytic continuation of $M_{--}(z_{\mathbf{q}}, \mathbf{q})$ is therefore given by

$$M_{--}^{\downarrow}(z_{\mathbf{q}}, \mathbf{q}) = \begin{cases} -iN_0 \frac{v_\mu q}{2\Delta} \sqrt{\zeta} E\left(\frac{1}{\sqrt{\zeta}}\right), & \mathrm{Im}(\zeta) > 0 \\ -iN_0 \frac{v_\mu q}{2\Delta} \sqrt{\zeta} \Big\{E\left(\frac{1}{\sqrt{\zeta}}\right) \\ \quad + 2i[E(\sqrt{1 - \zeta^{-1}}) - K(\sqrt{1 - \zeta^{-1}})]\Big\}, & \mathrm{Im}(\zeta) < 0. \end{cases} \tag{22}$$

We use the same tactics to compute $M_{++}(z_{\mathbf{q}}, \mathbf{q})$, given by

$$M_{++}(z, \mathbf{q}) = \frac{1}{2} \int \frac{d^2 p}{(2\pi)^2} \left(\frac{E_+ + E_-}{E_+ E_-} \frac{\xi_+ \xi_- + E_+ E_- + \Delta^2}{z^2 - (E_+ + E_-)^2} + \frac{1}{E} \right). \tag{23}$$

Evaluating the momentum integral in the same way as for $M_{--}(z_{\mathbf{q}}, \mathbf{q})$, we obtain

$$M_{++}(z_{\mathbf{q}}, \mathbf{q}) = -iN_0 \frac{2\Delta}{v_\mu q} \frac{1}{\sqrt{\zeta}} K\left(\frac{1}{\sqrt{\zeta}}\right), \tag{24}$$

where $K(z)$ is the complete elliptic integral of the first kind. The analytical continuation through the interval of the real axis where $\zeta \in (0, 1)$ is achieved by substituting $K(\frac{1}{\sqrt{\zeta}})$ at $\mathrm{Im}(\zeta) = 0^+$ by $K(\frac{1}{\sqrt{\zeta}}) - 2iK(\sqrt{1 - \zeta})\sqrt{\zeta}$ when $\mathrm{Im}(\zeta) < 0$ (see Sec. D of the SM [42]). We then obtain

$$M_{++}^{\downarrow}(z_{\mathbf{q}}, \mathbf{q}) = \begin{cases} -iN_0 \frac{2\Delta}{v_\mu q} \frac{1}{\sqrt{\zeta}} K\left(\frac{1}{\sqrt{\zeta}}\right), & \mathrm{Im}(\zeta) > 0 \\ -iN_0 \frac{2\Delta}{v_\mu q} \frac{1}{\sqrt{\zeta}} [K\left(\frac{1}{\sqrt{\zeta}}\right) - 2iK(\sqrt{1 - \zeta})\sqrt{\zeta}], & \mathrm{Im}(\zeta) < 0. \end{cases} \tag{25}$$

We now turn to the matrix elements $M_{+-}(z, \mathbf{q})$ and $M_{-+}(z, \mathbf{q})$, which couple amplitude and phase fluctuations. Since $M_{-+}(z, \mathbf{q}) = -M_{+-}(z, \mathbf{q})$, we focus on $M_{+-}(z, \mathbf{q})$. We recall that, in the end, we need to solve $\det \hat{M}^{\downarrow}(z_{\mathbf{q}}, \mathbf{q}) = M_{++}^{\downarrow}(z_{\mathbf{q}}, \mathbf{q}) M_{--}^{\downarrow}(z_{\mathbf{q}}, \mathbf{q}) - M_{+-}^{\downarrow}(z_{\mathbf{q}}, \mathbf{q}) M_{-+}^{\downarrow}(z_{\mathbf{q}}, \mathbf{q}) = 0$. At small $\mathbf{q}$ we have $M_{++}(z_{\mathbf{q}}, \mathbf{q}) = O(1/q)$ and $M_{--}(z_{\mathbf{q}}, \mathbf{q}) = O(q)$. Since their product is $O(1)$, it is sufficient to compute $M_{+-}(z_{\mathbf{q}}, \mathbf{q})$ at $q = 0$, where $z_{\mathbf{q}=0} = 2\Delta$. The matrix element $M_{+-}(2\Delta, 0)$ is purely imaginary and is given by

$$M_{+-}(2\Delta, 0) = i\frac{\Delta}{2} N_0 \int_{-\mu}^{\infty} \frac{d\xi}{\xi E} \tag{26}$$

$$= i\frac{N_0}{4} \ln\left(\frac{\sqrt{\mu^2 + \Delta^2} + \Delta}{\sqrt{\mu^2 + \Delta^2} - \Delta}\right). \tag{27}$$

A. High-density limit

In the high-density limit where $\mu \approx E_F \gg \Delta$, the amplitude-phase coupling arising from M_{+-} is small in Δ/μ and can be neglected. The Higgs susceptibility $\chi_H^{\downarrow}(z, \mathbf{q})$ then reduces to $\chi_H^{\downarrow}(z, \mathbf{q}) = 1/M_{--}^{\downarrow}(z, \mathbf{q})$. The parameter ζ, which

---

[2]To be explicit, here we use the convention where the complete elliptic integrals of first and second kind are defined as $K(z) = \int_0^{\pi/2} dx/(1 - z^2 \cos^2 x)^{1/2}$ and $E(z) = \int_0^{\pi/2} dx(1 - z^2 \cos^2 x)^{1/2}$ [see Eq. (19.2.8) of Ref. [50]]. This is different from the convention used in *Mathematica*, where z^2 in the integrands of $K(z)$ and $E(z)$ are replaced by z.

determines the location of the Higgs mode in the lower half plane is the solution of $M^\downarrow_{--}(\zeta) = 0$, i.e., of

$$E\left(\frac{1}{\sqrt{\zeta}}\right) + 2i\left[E\left(\sqrt{1-\zeta^{-1}}\right) - K\left(\sqrt{1-\zeta^{-1}}\right)\right] = 0. \quad (28)$$

The solution of this transcendental equation is $\zeta = 0.5 - 0.4302i$, so that the location of the Higgs mode is

$$z_\mathbf{q} = 2\Delta + (0.5 - 0.4302i)\frac{q^2}{2m}\frac{\mu}{\Delta}. \quad (29)$$

The dispersion of the Higgs mode at small $\mathbf{q}$ is given by $\omega_\mathbf{q} = \text{Re}(z_\mathbf{q}) = 2\Delta + (q^2/4m)(\mu/\Delta)$. The damping rate of the Higgs mode, $\gamma_\mathbf{q}$, is quadratic in $\mathbf{q}$, as in 3D [41,43].

B. Away from the high-density limit

Away from the high-density limit, M_{+-} has to be kept. The susceptibility $\chi^\downarrow_H(z_\mathbf{q}, \mathbf{q})$ has the form

$$\chi^\downarrow_H(z_\mathbf{q}, \mathbf{q}) = \frac{i}{N_0}\frac{2\Delta}{v_\mu q}\frac{1}{\sqrt{\zeta}}$$

$$\times \frac{K\left(\frac{1}{\sqrt{\zeta}}\right) - 2iK(\sqrt{1-\zeta})\sqrt{\zeta}}{\left[K\left(\frac{1}{\sqrt{\zeta}}\right) - 2iK(\sqrt{1-\zeta})\sqrt{\zeta}\right]\left\{E\left(\frac{1}{\sqrt{\zeta}}\right) + 2i[E(\sqrt{1-\zeta^{-1}}) - K(\sqrt{1-\zeta^{-1}})]\right\} + \frac{1}{16}\left[\ln\left(\frac{\sqrt{\mu^2+\Delta^2}+\Delta}{\sqrt{\mu^2+\Delta^2}-\Delta}\right)\right]^2}.$$

$$(30)$$

The position of the Higgs mode is determined by the condition

$$\left[K\left(\frac{1}{\sqrt{\zeta}}\right) - 2iK\left(\sqrt{1-\zeta}\right)\sqrt{\zeta}\right]\left\{E\left(\frac{1}{\sqrt{\zeta}}\right) + 2i[E(\sqrt{1-\zeta^{-1}}) - K(\sqrt{1-\zeta^{-1}})]\right\} + \frac{1}{16}\left[\ln\left(\frac{\sqrt{\mu^2+\Delta^2}+\Delta}{\sqrt{\mu^2+\Delta^2}-\Delta}\right)\right]^2 = 0. \quad (31)$$

We numerically solve this equation for ζ for any value of Δ and $\mu > 0$, where this equation is valid. We present the results in Fig. 5. We see that ζ evolves as a function of μ, but, remarkably, $\text{Re}(\zeta) = 0.5$ for *all* values of μ. With this, the dispersion at small $\mathbf{q}$ is given for all μ by $\omega(\mathbf{q}) = 2\Delta + (q^2/4m)(\mu/\Delta)$.

The fact that $\text{Re}(\zeta) = 0.5$ holds for all $\mu > 0$ follows from a special reflection symmetry of the equation for the pole location in 2D. We show in Sec. E of the SM that, if ζ is a solution to Eq. (31), its reflection across the line where $\text{Re}(\zeta) = 0.5$ is also a solution [42]. Combining this with the empirical fact that Eq. (31) has a unique solution, we immediately find that $\text{Re}(\zeta)$ must equal 0.5 for all values of μ.[3] We see therefore that $\text{Re}(\zeta)$ remains inside the interval (0,1) for any positive value of μ. This is in contrast with the behavior in 3D, where $\text{Re}(\zeta)$ becomes negative for $\mu < \mu_c = 0.8267\Delta$ [43].

The damping rate of the Higgs mode increases with decreasing μ and diverges in the limit where $\mu \ll \Delta$ as

$$\text{Im}(\zeta) \approx -i\frac{e}{16}\sqrt{\frac{2\Delta}{\mu}}. \quad (32)$$

In the inset of Fig. 5, we overlay this expression on the numerical solution of Eq. (31), finding good agreement for smaller values of μ/Δ.

Although $\text{Im}(\zeta)$ diverges as μ approaches zero, we find that the Higgs resonance does not become overdamped at small μ. To see this, recall that the dispersion of the Higgs mode is given by $z_\mathbf{q} = 2\Delta + \zeta(q^2/2m)(\mu/\Delta)$. As such, at $\mu \ll \Delta$, we have $-\text{Im}(z_\mathbf{q})/\text{Re}(z_\mathbf{q}) \sim \frac{q^2}{m\Delta}\sqrt{\frac{\mu}{\Delta}} \ll 1$. From this, we find that the Higgs mode leads to a well-defined resonance at all values of $\mu > 0$.
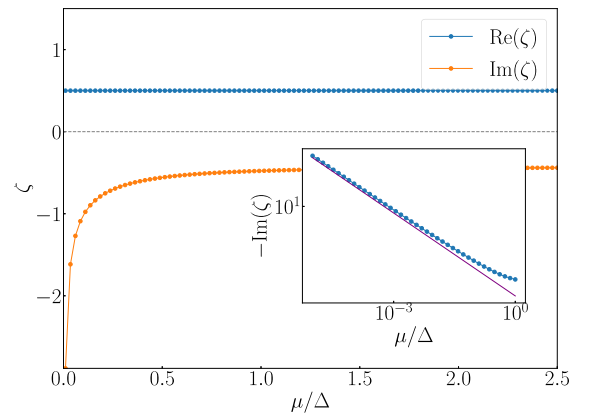
FIG. 5. The real and imaginary parts of ζ given by the solution of Eq. (31), as a function of μ. The quantity ζ is related to the dispersion of the Higgs mode as $\omega_\mathbf{q} = 2\Delta + \zeta(q^2/2m)(\mu/\Delta)$. We see that $\text{Re}(\zeta) = 0.5$ for all μ/Δ, while $\text{Im}(\zeta)$ diverges at small μ. The inset highlights that the divergence is a power-law. The purple line in the inset is the analytical expression for $\text{Im}(\zeta)$, Eq. (32).

_____

[3]That Eq. (31) has a unique solution can be intuited by counting degrees of freedom: since there are two degrees of freedom in our system (corresponding to phase and amplitude fluctuations), we expect two collective modes. By looking for a collective mode with dispersion $z_\mathbf{q} = 2\Delta + \zeta(q^2/2m)(\mu/\Delta)$, we explicitly disregard the ABG mode and focus on the Higgs mode near 2Δ. This Higgs mode should result in one solution for Eq. (31).

C. The residue of the Higgs mode

The residue of the Higgs mode is defined as $Z_{\mathbf{q}} = \lim_{z \to z_{\mathbf{q}}}(z - z_{\mathbf{q}})\chi_H^{\downarrow}(z, \mathbf{q})$. We find

$$Z_{\mathbf{q}} = i\frac{v_\mu q}{2N_0} \frac{\frac{1}{\sqrt{\zeta}}K\left(\frac{1}{\sqrt{\zeta}}\right) - 2iK(\sqrt{1-\zeta})}{\frac{d}{d\zeta}\left[K\left(\frac{1}{\sqrt{\zeta}}\right) - 2iK(\sqrt{1-\zeta})\sqrt{\zeta}\right]\left\{E\left(\frac{1}{\sqrt{\zeta}}\right) + 2i[E(\sqrt{1-\zeta^{-1}}) - K(\sqrt{1-\zeta^{-1}})]\right\}}, \tag{33}$$

where ζ is the solution of Eq. (31).

As expected, $Z_{\mathbf{q}}$ goes to zero in the long-wavelength limit. This reflects the disappearance of the pole in the susceptibility $\chi_H(z, \mathbf{q})$ at $\mathbf{q} = 0$. At high density, $Z_{\mathbf{q}} = -0.2474(1 - i)v_F q/N_0$. In the opposite limit where $\mu/\Delta \to 0$,

$$Z_{\mathbf{q}} \approx -\frac{(1-i)e^{1/2}}{16}\frac{v_\Delta q}{N_0}\left(\frac{\mu}{2\Delta}\right)^{1/4} \tag{34}$$

up to logarithmic corrections. Here, v_Δ is defined through $mv_\Delta^2/2 = \Delta$. From this expression, we see that the residue of the pole goes to zero at small μ as $(\mu/\Delta)^{1/4}$. In Fig. 6, we plot $|Z_{\mathbf{q}}|/q$ at small $\mathbf{q}$, using both the exact expression of Eq. (33) and the approximate expression of Eq. (34), including logarithmic corrections to Eq. (34). From Fig. 6, we see that there is good agreement between the exact and approximate expressions for $Z_{\mathbf{q}}$ at small μ/Δ.

Although we focus on the residue of the Higgs pole in $\chi_H^{\downarrow}(z, \mathbf{q})$, this pole also appears in the susceptibilities $\chi_{++}^{\downarrow}(z, \mathbf{q})$ and $\chi_{+-}^{\downarrow}(z, \mathbf{q})$, which correspond to the correlation functions $\langle|\theta(q)|^2\rangle$ and $\langle\theta^*(q)\lambda(q)\rangle$, respectively. Analogous to the above calculation, one can obtain the residue of the pole for $\chi_{++}^{\downarrow}(z, \mathbf{q})$ and $\chi_{+-}^{\downarrow}(z, \mathbf{q})$.

After doing so, one finds that the residue of the pole in $\chi_H^{\downarrow}(z, \mathbf{q})$ is much larger than the residue of the pole in $\chi_{++}^{\downarrow}(z, \mathbf{q})$ and $\chi_{+-}^{\downarrow}(z, \mathbf{q})$ (by a factor of q^2 and q, respectively.) In other words, the pole at $z_{\mathbf{q}}$ mainly leads to a peak in the channel corresponding to amplitude fluctuations, not phase fluctuations. This is true for all values of $\mu > 0$. This does not contradict the fact that there is indeed phase-amplitude mixing at all $\mu > 0$, as evinced by the fact that $M_{+-}(z, \mathbf{q}) \neq 0$. These conclusions agree with previous results obtained in three dimensions [43,45].

In Sec. VII, we show that amplitude and phase fluctuations are decoupled at small $\mathbf{q}$ when the Coulomb interaction is taken into account. In that case, the pole at $z_{\mathbf{q}}$ is clearly only attributable to amplitude fluctuations.

D. Susceptibility $\chi_H(\omega, \mathbf{q})$ along the real axis

To calculate the observable $\text{Im}\chi_H(\omega + i\delta, \mathbf{q})$, we recall that for $\zeta \in (0, 1)$, $\chi_H(\omega + i\delta, \mathbf{q}) = \chi_H^{\downarrow}(\omega, \mathbf{q})$. Near the location of the pole in the lower half plane, we can write $\chi_H^{\downarrow}(z, \mathbf{q}) = A + Z_{\mathbf{q}}/(z - \omega_{\mathbf{q}} + i\gamma_{\mathbf{q}})$. If the pole is close to the real axis, we then expect the spectral function $\text{Im}\chi_H(\omega + i\delta, \mathbf{q})$ to be approximately given by $\text{Im}(A) + \text{Im}[Z_{\mathbf{q}}/(\omega - \omega_{\mathbf{q}} + i\gamma_{\mathbf{q}})]$. This has a peak at $\omega = \omega_{\mathbf{q}}$, and an approximate width of $\gamma_{\mathbf{q}}$.

In Fig. 7(a), we plot the spectral function $\text{Im}\chi_H(\omega + i\delta, \mathbf{q})$ obtained numerically using Eqs. (10)–(16) for five momenta between $q = 0$ and $q = 0.1k_F$, using $\delta = 10^{-5}\Delta$ and $E_F = 10E_0$ (corresponding to $\mu/\Delta \approx 1.42$). The overlaid dashed black lines are the curves obtained by fitting $\text{Im}\chi_H(\omega + i\delta, \mathbf{q})$ to the function $C + \text{Im}[Z_{\mathbf{q}}/(\omega - \omega_{\mathbf{q}} + i\gamma_{\mathbf{q}})]$. Since we expect this functional form to only be meaningful near the resonance of the spectral function, we restrict each fit to only use data points where $\text{Im}\chi_H(\omega + i\delta, \mathbf{q}) > 0.8\max(\text{Im}\chi_H(\omega + i\delta, \mathbf{q}))$.

We see that, at small $\mathbf{q}$, $\text{Im}\chi_H(\omega + i\delta, \mathbf{q})$ closely resembles the one-sided square-root singularity we expect from $q = 0$, albeit with a peak above 2Δ. With increasing q, this peak in the spectral function broadens substantially and moves to larger values of ω. In Figs. 7(b) and 7(c), we present the extracted values of $\omega_{\mathbf{q}}$, $\gamma_{\mathbf{q}}$ and $|Z_{\mathbf{q}}|$ from fitting each of the five curves. We have also added a dashed gray curve to denote the results expected from the analytical expressions derived above. We find good agreement in the dispersion $\omega_{\mathbf{q}}$ and damping rate $\gamma_{\mathbf{q}}$, while the agreement between the numerical and analytical results for $|Z_{\mathbf{q}}|$ is a bit more ambiguous.

In particular, the values of $|Z_{\mathbf{q}}|$ extracted from fitting to the numerical data consistently lie above the line expected from our analytical results. We attribute this to the ambiguity in the method used to fit the data: although we restrict each fit to only use data points above some threshold, $\text{Im}\chi_H(\omega + i\delta, \mathbf{q}) > 0.8\max(\text{Im}\chi_H(\omega + i\delta, \mathbf{q}))$, this 80% threshold is rather arbitrary. We find that the values of $|Z_{\mathbf{q}}|$ extracted from fitting to the data are rather sensitive to the precise threshold used.[4] Nonetheless, we find that the values of $|Z_{\mathbf{q}}|$ extracted from fitting to the data agree with the analytical results within a factor of ≈ 2 for all reasonable thresholds. Moreover, we find that, for all thresholds employed, (i) $|Z_{\mathbf{q}}|$ increases linearly with q, and (ii) the phase of $Z_{\mathbf{q}}$, i.e., $\arg(Z_{\mathbf{q}})$, is approximately
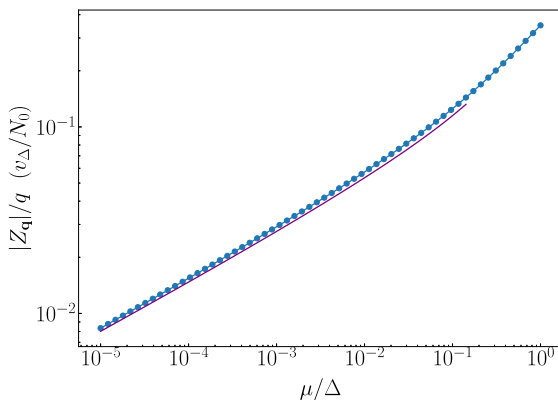

FIG. 6. The ratio $|Z_{\mathbf{q}}|/q$ as a function of μ/Δ, Eq. (33). The purple line is an approximate analytic expression at small μ/Δ: $|Z_{\mathbf{q}}|/q \propto (\mu/2\Delta)^{1/4}$, Eq. (34).

---

[4]$\omega_{\mathbf{q}}$ and $\gamma_{\mathbf{q}}$ also change with the threshold but continue to fit the analytical expressions relatively well regardless of the precise threshold used.
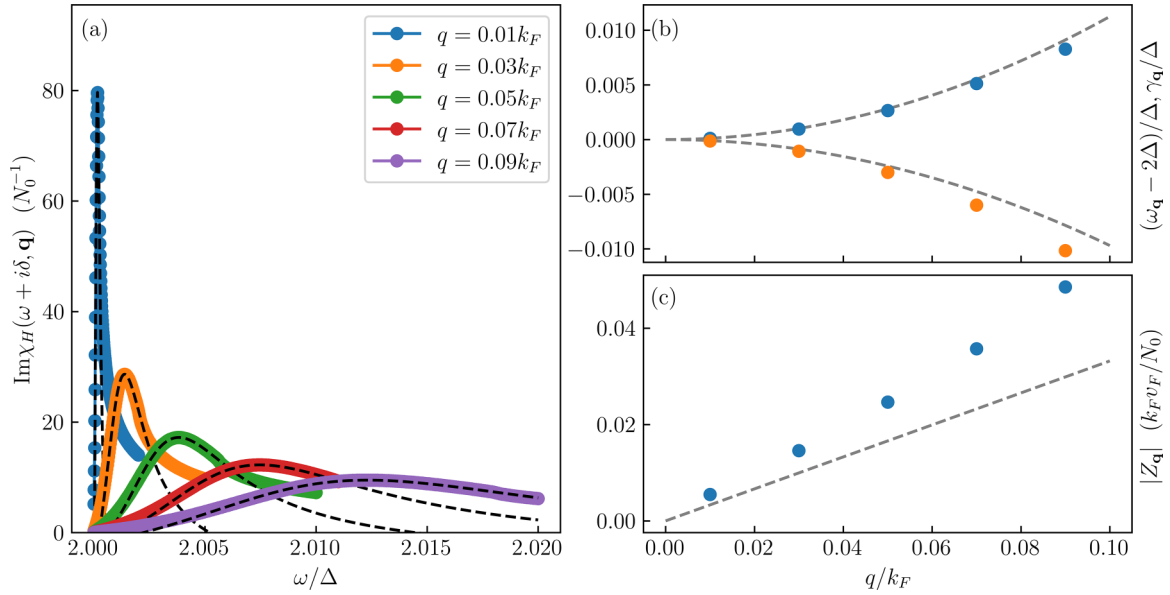
FIG. 7. (a) The spectral function $\mathrm{Im}\chi_H(\omega + i\delta, \mathbf{q})$ as a function of ω for different values of $\mathbf{q}$ at $E_F = 10E_0$ ($\mu = 9E_0$, $\Delta = 2\sqrt{10}E_0$, $\mu/\Delta = 1.42$), setting $\delta = 10^{-5}\Delta$. The dashed black lines are the fits to $\mathrm{Im}\chi_H(\omega + i\delta, \mathbf{q}) = C + \mathrm{Im}[Z_\mathbf{q}/(\omega - \omega_\mathbf{q} + i\gamma_\mathbf{q})]$. (b), (c) The behavior of $\omega_\mathbf{q}$, $\gamma_\mathbf{q}$, and $|Z_\mathbf{q}|$ as a function of $\mathbf{q}$, extracted from the fits in panel (a). The dashed gray curves correspond to our analytical expressions.

$3\pi/4$. Both behaviors agree with the analytical expressions in Eqs. (33) and (34).

We note in passing that our result that the peak in $\mathrm{Im}\chi_H(\omega + i\delta, \mathbf{q})$ in 2D exists for all $\mu > 0$ (in contrast with 3D, where the peak only exists for $\mu > 0.8267\Delta$), agrees with a previous numerical study, which found that the Higgs mode is more visible in the dynamical structure factor in 2D compared with 3D [51]. We also note that, as $\mu \to 0$, the boundary frequency $\omega_2 = 2\Delta + (q^2/2m)(\mu/\Delta)$ approaches 2Δ, i.e., the interval $(2\Delta, \omega_2)$ vanishes at $\mu = 0$. This is in line with the vanishing of the residue of the Higgs mode $Z_\mathbf{q} \sim (\mu/\Delta)^{1/4}$ as $\mu \to 0$.

V. THE HIGGS MODE AT LARGER VALUES OF q

So far, we have analyzed the Higgs mode at small $\mathbf{q}$. In this section, we go beyond the small-$\mathbf{q}$ regime, continuing to take $\mu > 0$. We find how the Higgs mode evolves as a function of $\mathbf{q}$ by numerically solving for the position of the pole of $\chi_H^\downarrow(z, \mathbf{q})$ without assuming that q is small (see Sec. C of the SM for details [42]). Our results are shown in Fig. 8 for $E_F = 10E_0$.

In Fig. 8(a), we show how the pole of $\chi_H^\downarrow(z, \mathbf{q})$ moves through the lower half plane as a function of q. With increasing q, the pole at $z_\mathbf{q}$ quickly moves away from the real axis, leading to heavier damping of the Higgs mode. As q increases beyond some threshold q_c, $\mathrm{Re}(z_\mathbf{q})$ becomes larger than ω_2. In this situation, $\chi_H^\downarrow(z, \mathbf{q})$ is no longer continuous upon crossing the real axis. At this point, the pole in the lower half plane becomes a hidden mode—although the pole exists, it does not lead to a peak in $\mathrm{Im}\chi_H(\omega + i\delta, \mathbf{q})$ since it lies below a branch cut of $\chi_H^\downarrow(z, \mathbf{q})$. To highlight this transition, we mark the point where the Higgs mode becomes hidden with a red diamond. For $q < q_c$, the Higgs mode is observable; we highlight these values via a light-orange background. Similarly, the Higgs

mode is hidden for $q > q_c$, and we highlight this region with a light-blue background.

In Fig. 8(b), we present the spectral function $\mathrm{Im}\chi_H(\omega + i\delta, \mathbf{q})$, as well as the dispersion of the Higgs mode, $\mathrm{Re}(z_\mathbf{q})$, obtained by numerically solving $\det \hat{M}(z_\mathbf{q}, \mathbf{q}) = 0$ for all $\mathbf{q}$. Additionally, we added a hatched region corresponding to $(2\Delta, \omega_2)$—values of $\mathrm{Re}(z_\mathbf{q})$ in this region are not hidden below a branch cut and lead to a peak in the spectral function. From this plot, we see a sharp bright feature in the spectral function near $z = 2\Delta$ and $q = 0$, which broadens with q. The peak in $\mathrm{Im}\chi_H(\omega + i\delta, \mathbf{q})$ disappears around $q = 1.1k_F$, where $\mathrm{Re}(z_\mathbf{q})$ becomes larger than ω_2. This behavior is fully consistent with Fig. 8(a), where the pole moves with increasing q deeper into the lower half plane and is eventually hidden below a branch cut. As in Fig. 8(a), we highlight the moment where the pole becomes hidden with a red diamond. Also visible in Fig. 8(b) is the ABG mode, which disperses linearly at small q. Its visibility in the Higgs (amplitude) susceptibility arises from the phase-amplitude coupling, which is nonzero at finite μ/Δ.

VI. THE HIGGS MODE FOR $\mu < 0$

Thus far, we have restricted ourselves to the case where $\mu > 0$. In this section, we consider the behavior of the Higgs mode for $\mu < 0$. For this analysis, we first note that both ω_2 and ω_3, depicted in Fig. 4, approach 2Δ as μ approaches zero from above. At $\mu = 0$, $\omega_2 = \omega_3 = 2\Delta$, and the interval $(2\Delta, \infty)$ coincides with the interval (ω_3, ∞). A simple analysis shows that, for $\mu < 0$, the frequency $\omega_3 = 2[\Delta^2 + (|\mu| + q^2/8m)^2]^{1/2}$ becomes the lower boundary for the branch cut in $\chi_H(\omega, \mathbf{q})$, $\omega_{\min}$, i.e., a branch cut exists for $\omega > \omega_3 = \omega_{\min}$.

This change in the branch-cut boundary can also be understood by thinking of 2Δ, ω_2, and ω_3 as branch points of the Higgs susceptibility. From this perspective, the branch points
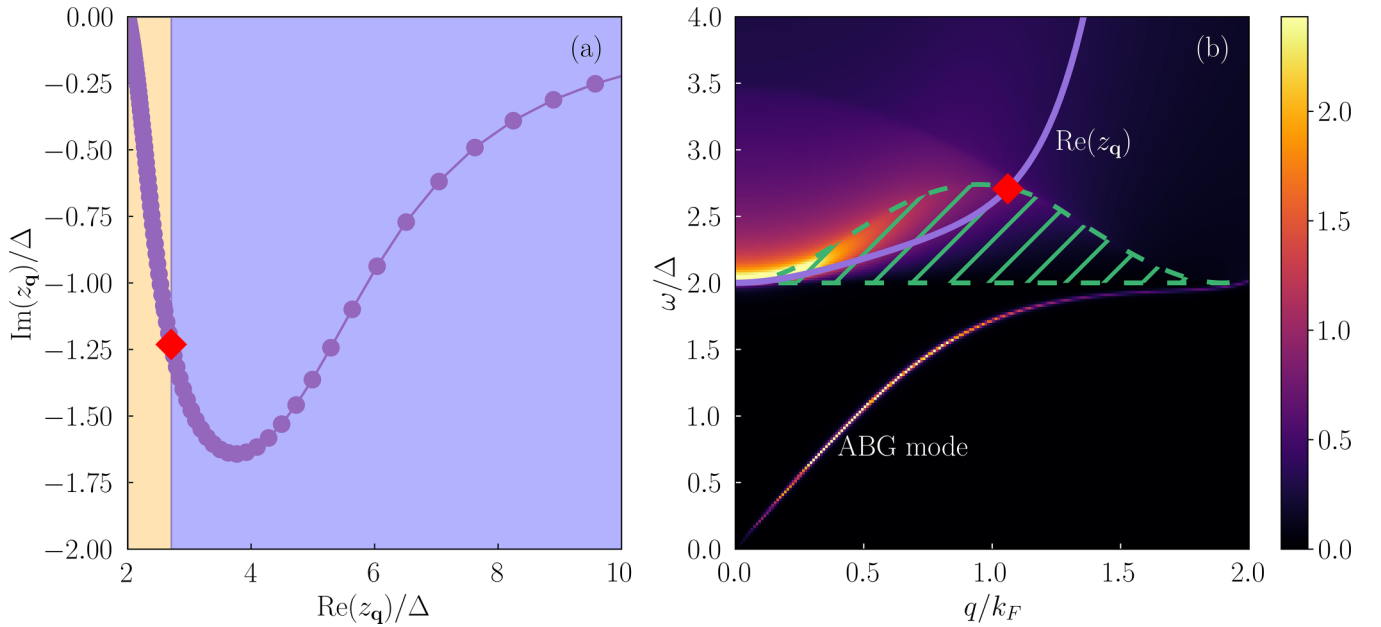
FIG. 8. The location of the pole and the spectral function $\text{Im}\chi_H(\omega + i\delta, \mathbf{q})$ in the BCS regime at $E_F = 10E_0$ ($\mu = 9E_0$, $\Delta = 2\sqrt{10}E_0$, and $\mu/\Delta = 1.42$). (a) The path of the pole of $\chi_H^\downarrow(z, \mathbf{q})$ through the lower half plane with increasing q. For $q > q_c = 1.08k_F$, the pole is hidden below a branch cut, and does not lead to a resonance in the spectral function $\text{Im}\chi_H(\omega + i\delta, \mathbf{q})$. The transition point where the pole becomes hidden is marked with a red diamond. We highlight the region where a pole leads to a peak in $\text{Im}\chi_H(\omega + i\delta, \mathbf{q})$ with a light-orange background, and the region where the pole is hidden below a branch cut with a light-blue background. (b) The spectral function $\text{Im}\chi_H(\omega + i\delta, \mathbf{q})$ (color-coding on the right), using $\delta = 10^{-5}\Delta$. Purple line—$\text{Re}(z_\mathbf{q})$, where $z_\mathbf{q}$ is the position of the pole of $\chi_H^\downarrow(z, \mathbf{q})$. The hatched green region corresponds to frequencies between 2Δ and ω_2. The two frequencies differ by q^2 at small q and merge again at $q = 2\sqrt{2m\mu}$. Values of $\text{Re}(z_\mathbf{q})$ in the hatched region correspond to those in the light-orange region in panel (a). Outside this region, the pole is hidden. The data show that the peak inside the hatched region rapidly broadens with increasing q. The mode below 2Δ in panel (b) is the ABG mode.

2Δ and ω_2 annihilate at $\mu = 0$, leaving only the branch point at ω_3 for $\mu < 0$. Mathematically, the disappearance of the branch points at 2Δ and ω_2 as μ changes sign corresponds to a change in the topology of the Riemann surface at $\mu = 0$.

To search for a resonance in the susceptibility $\chi_H(\omega + i\delta, \mathbf{q})$, we now investigate its analytical continuation through the real axis at $\omega > \omega_3$ and search for a pole in $\chi_H^\downarrow(z, \mathbf{q})$ in the lower half plane. Skipping the details of the calculations, we find that a pole exists at some $z = z_\mathbf{q}$, but $\text{Re}(z_\mathbf{q}) < \omega_3$. That is, the pole at $\mu < 0$ is hidden, since $\chi_H^\downarrow(z, \mathbf{q})$ is discontinuous across the real axis at $\omega = \text{Re}(z_\mathbf{q})$. We therefore expect that this pole does not lead to a peak in $\text{Im}\chi_H(\omega + i\delta, \mathbf{q})$.

Our results, presented in Fig. 9, confirm this. As in Fig. 8(a), we plot the spectral function $\text{Im}\chi_H(\omega + i\delta, \mathbf{q})$ and overlay $\text{Re}(z_\mathbf{q})$, where $z_\mathbf{q}$ is the position of the pole of $\chi_H^\downarrow(z, \mathbf{q})$ in the lower half plane. We see from Fig. 9 that the Higgs mode is relatively nondispersive: for all q which we study, the real part of the pole lies near 2Δ. Although the position of the pole is only presented in Fig. 9 for $q \lesssim 0.3k_F$, we find that the pole stays near $z = 2\Delta$ for larger values of q. The absence of pole positions for larger q in Fig. 9 is due to numerical difficulties.[5]

---

[5]We obtain the position of the pole in $\chi_H^\downarrow(z, \mathbf{q})$ by solving $\det \hat{M}^\downarrow(z_\mathbf{q}, \mathbf{q}) = 0$ using Newton's method. For poles sufficiently close to the real-frequency axis, we find that Newton's method does not converge. This possible failure of Newton's method for finding complex roots is well known [53].
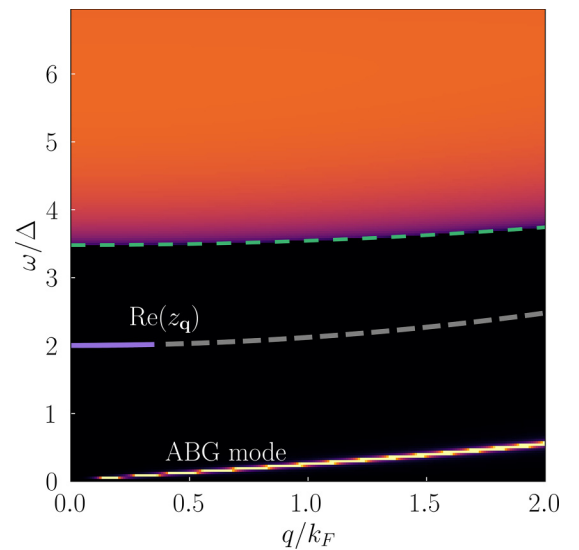

FIG. 9. $\text{Im}\chi_H(\omega + i\delta, \mathbf{q})$ in the BEC regime, at $E_F = 0.1E_0$ ($\mu = -0.9E_0$, $\Delta = 0.63E_0$, and $\mu/\Delta = -1.42$) and $\delta = 10^{-5}\Delta$. The color coding is the same as in Fig. 8. The dashed green curve is the edge of the two-particle continuum, which at finite q is $\omega_{\min} = 2[\Delta^2 + (|\mu| + q^2/8m)^2]^{1/2}$. The purple line shows $\text{Re}(z_\mathbf{q})$, where $z_\mathbf{q}$ is the location of the pole of $\chi_H^\downarrow(z, \mathbf{q})$. This $\text{Re}z_\mathbf{q}$ is obtained numerically by solving $\det \hat{M}^\downarrow(z_\mathbf{q}, \mathbf{q}) = 0$ for each value of $\mathbf{q}$. The pole positions at larger q are not shown due to numerical difficulties [52]. Although the pole is below the edge of the continuum, it leads to a hidden mode and no peak in $\text{Im}\chi_H(\omega + i\delta, \mathbf{q})$ (see text). The peak in $\text{Im}\chi_H(\omega + i\delta, \mathbf{q})$ at small ω corresponds to the ABG mode.

We see from the figure that $\text{Im}\chi_H(\omega + i\delta, \mathbf{q})$ does not display any peak. This is consistent with the hidden nature of the Higgs mode. The disappearance of the observable Higgs peak in the BEC regime, where $\mu < 0$, agrees with previous theoretical results in 3D [43,54], experimental results for 3D cold-atom systems [39], and numerical studies in 2D [51]. As in the case of positive μ, the ABG mode is visible below the two-particle continuum. Compared with Fig. 8, the dispersion of the ABG mode is much flatter than for $\mu > 0$. This can be understood from the mean-field dispersion of the ABG mode, $\omega_{\text{ABG}}(q) = cq$ where $c = v_F/\sqrt{2}$ [55]. Since the velocity of the ABG mode is proportional to v_F, the dispersion of the ABG mode becomes flatter as the density decreases.

VII. INCLUDING THE COULOMB INTERACTION

We now extend our analysis to account for the effects of the long-range Coulomb interaction. To do so, we return to the action. Extending Eq. (1) to include the Coulomb interaction, we have

$$
\begin{aligned}
S[\bar{\psi}, \psi] = & \sum_k \bar{\psi}_{k\sigma}\left(-i\omega_n + \frac{k^2}{2m} - \mu\right)\psi_{k\sigma} \\
& - g\frac{T}{L^2}\sum_{kqp}\bar{\psi}_{k+q/2\uparrow}\bar{\psi}_{-k+q/2\downarrow}\psi_{-p+q/2\downarrow}\psi_{p+q/2\uparrow} \\
& + \frac{T}{2L^2}\sum_{pkq}\bar{\psi}_{p+q\sigma}\bar{\psi}_{k-q\sigma'}V_c(\mathbf{q})\psi_{k\sigma'}\psi_{p\sigma},
\end{aligned}
\tag{35}
$$

where the Coulomb interaction in two dimensions is $V_c(\mathbf{q}) = 2\pi e^2/q$. To decouple the quartic terms, we introduce two Hubbard-Stratonovich fields, Δ and Φ for the particle-particle and particle-hole channels, respectively. The mean-field equations for Δ and Φ, $\delta S/\delta\Delta = 0$ and $\delta S/\delta\Phi = 0$, yield $\Phi = 0$ and an unchanged gap equation Eq. (4). Similarly, the constraint of particle-number conservation yields Eq. (5), as in the neutral case. Then we still have $\mu = E_F - E_0$ and $\Delta = 2\sqrt{E_F E_0}$.

Of course, in reality the Coulomb repulsion does affect μ and Δ: it certainly weakens a system's tendency toward s-wave superconductivity [47,56–58] and may also lead to superconducting instabilities in non-s-wave channels [59,60]. That μ and Δ are unaffected by the repulsive Coulomb interaction in our calculation follows from the fact that we decouple the Coulomb interaction in the particle-hole channel but not in the particle-particle channel. This is an approximation which we use simply because our goal is to analyze the effect of the Coulomb interaction on the Higgs mode.

To include fluctuations, we introduce as before the amplitude and phase fluctuation fields $\lambda(x)$ and $\theta(x)$. Additionally, we include fluctuations of $\Phi(x)$ about the mean field $\Phi = 0$. Expanding the action to quadratic order in λ_q, θ_q, and Φ_q and integrating out Φ_q following Ref. [33], we obtain the effective action in the form

$$
S_{\text{eff}} = S_0 + \beta\Delta^2 L^2 \sum_q \begin{pmatrix}\theta_q^* & \lambda_q^*\end{pmatrix}\hat{M}(i\Omega_m, \mathbf{q})\begin{pmatrix}\theta_q \\ \lambda_q\end{pmatrix},
\tag{36}
$$

where the matrix elements are now

$$
M_{++}(z, \mathbf{q}) = \frac{1}{g} + \frac{1}{2}\left(\chi_{22}(z, \mathbf{q}) - \frac{\chi_{23}(z, \mathbf{q})^2}{V_c^{-1}(\mathbf{q}) - \chi_{33}(z, \mathbf{q})}\right),
\tag{37}
$$

$$
M_{--}(z, \mathbf{q}) = \frac{1}{g} + \frac{1}{2}\left(\chi_{11}(z, \mathbf{q}) + \frac{\chi_{13}(z, \mathbf{q})^2}{V_c^{-1}(\mathbf{q}) - \chi_{33}(z, \mathbf{q})}\right),
\tag{38}
$$

$$
M_{+-}(z, \mathbf{q}) = \frac{1}{2}\left(\chi_{12}(z, \mathbf{q}) - \frac{\chi_{23}(z, \mathbf{q})\chi_{13}(z, \mathbf{q})}{V_c^{-1}(\mathbf{q}) - \chi_{33}(z, \mathbf{q})}\right).
\tag{39}
$$

The susceptibilities χ_{11}, χ_{22}, and χ_{12} are the same as in Eqs. (13), (14), and (15), respectively. The new susceptibilities χ_{33}, χ_{13}, and χ_{23}, which appear in the presence of the Coulomb interaction, are

$$
\chi_{33}(z, \mathbf{q}) = -2\int \frac{d^2p}{(2\pi)^2}\frac{E_+ + E_-}{2E_+E_-}\frac{\xi_+\xi_- - E_+E_- - \Delta^2}{z^2 - (E_+ + E_-)^2},
\tag{40}
$$

$$
\chi_{13}(z, \mathbf{q}) = 2\Delta\int \frac{d^2p}{(2\pi)^2}\frac{E_+ + E_-}{2E_+E_-}\frac{\xi_+ + \xi_-}{z^2 - (E_+ + E_-)^2},
\tag{41}
$$

$$
\chi_{23}(z, \mathbf{q}) = 2i\Delta z\int \frac{d^2p}{(2\pi)^2}\frac{E_+ + E_-}{2E_+E_-}\frac{1}{z^2 - (E_+ + E_-)^2}.
\tag{42}
$$

Our goal is to calculate the Higgs susceptibility $\chi_H(z, \mathbf{q}) = M_{++}(z, \mathbf{q},)/\det\hat{M}(z, \mathbf{q})$ at small but finite q. As in Sec. IV, we assume that the pole is at $z = z_{\mathbf{q}} = 2\Delta + \zeta(q^2/2m)(\mu/\Delta)$ and search for a solution of $\det\hat{M}(z_{\mathbf{q}}, \mathbf{q}) = 0$. We find (see Sec. F of the SM for details [42]) that at arbitrary $\mu > 0$, $M_{++}(z_{\mathbf{q}}, \mathbf{q})$ and $M_{--}(z_{\mathbf{q}}, \mathbf{q})$ are $O(q)$, while $M_{+-}(z_{\mathbf{q}}, \mathbf{q}) = O(q^2)$. From this, we see that the long-range Coulomb interaction effectively decouples the amplitude and phase oscillations in the long-wavelength limit, regardless of the value of μ/Δ. We then simply have

$$
\chi_H(z_{\mathbf{q}}, \mathbf{q}) \approx \frac{1}{M_{--}(z_{\mathbf{q}}, \mathbf{q})}.
\tag{43}
$$

To obtain $M_{--}(z_{\mathbf{q}}, \mathbf{q})$ at small $\mathbf{q}$, we set $\chi_{13}(z_{\mathbf{q}}, \mathbf{q}) \approx \chi_{13}(2\Delta, 0)$ and neglect $V_c^{-1}(\mathbf{q})$ compared with $\chi_{33}(z_{\mathbf{q}}, \mathbf{q})$, which is $O(1/q)$. Evaluating χ_{33} in the same way as in Sec. IV(see also Sec. A of the SM for a similar calculation [42]) and using our earlier result for $\chi_{11}(z_{\mathbf{q}}, \mathbf{q})$, we find

$$
\begin{aligned}
M_{--}(z_{\mathbf{q}}, \mathbf{q}) \approx & -iN_0\frac{2\Delta}{v_\mu q}\frac{\sqrt{\zeta}}{K\left(\frac{1}{\sqrt{\zeta}}\right)}\left[E\left(\frac{1}{\sqrt{\zeta}}\right)K\left(\frac{1}{\sqrt{\zeta}}\right)\right. \\
& \left. + \frac{1}{16}\ln\left(\frac{\sqrt{\Delta^2 + \mu^2} + \Delta}{\sqrt{\Delta^2 + \mu^2} - \Delta}\right)^2\right].
\end{aligned}
\tag{44}
$$

Analytically continuing $M_{--}(z_{\mathbf{q}}, \mathbf{q})$ into the lower half plane for $\zeta \in (0, 1)$ as we did in Sec. IV, we obtain the Higgs susceptibility $\chi_H^\downarrow(z_{\mathbf{q}}, \mathbf{q})$ in the presence of the

Coulomb interaction as

$$\chi_H^{\downarrow}(z_{\mathbf{q}}, \mathbf{q}) = \frac{i}{N_0} \frac{2\Delta}{v_\mu q} \frac{1}{\sqrt{\zeta}}$$

$$\times \frac{K\left(\frac{1}{\sqrt{\zeta}}\right) - 2iK(\sqrt{1-\zeta})\sqrt{\zeta}}{\left[K\left(\frac{1}{\sqrt{\zeta}}\right) - 2iK(\sqrt{1-\zeta})\sqrt{\zeta}\right]\left\{E\left(\frac{1}{\sqrt{\zeta}}\right) + 2i[E(\sqrt{1-\zeta^{-1}}) - K(\sqrt{1-\zeta^{-1}})]\right\} + \frac{1}{16}\left[\ln\left(\frac{\sqrt{\mu^2+\Delta^2}+\Delta}{\sqrt{\mu^2+\Delta^2}-\Delta}\right)\right]^2}. \quad (45)$$

This is exactly the same equation for ζ as Eq. (30) in the absence of the Coulomb interaction. From this, we see that, although the Coulomb interaction drastically modifies the character of the phase oscillations, transforming the ABG mode into the plasmon, the Higgs mode is *unaffected* by the presence of the long-range Coulomb interaction. A similar calculation shows that the Higgs mode is also unaffected by the long-range Coulomb interaction in 3D.

This result is unintuitive, since the presence of Coulomb interaction leads to a decoupling of amplitude and phase oscillations at all μ/Δ. Hence, one might reasonably expect the Higgs mode to behave substantially differently in the charged system compared with a neutral superfluid. It is therefore remarkable that the location of the Higgs mode is identical in both the neutral and charged systems.

We verify these analytical results by numerically calculating the spectral function $\text{Im}\chi_H(\omega + i\delta, \mathbf{q})$ in the charged system. For these calculations, we employ the dimensionless Wigner-Seitz radius, $r_s = 1/(\pi n a_0^2)^{1/2}$, where n is the fermionic density and $a_0 = 1/me^2$ is the Bohr radius. Recalling that $k_F = \sqrt{2\pi n}$, the Coulomb interaction in terms of r_s is $V_c(q) = 2\pi e^2/q = r_s/(\sqrt{2}N_0\bar{q})$, where $\bar{q} = q/k_F$. In our numerical calculations, we set $r_s = 1$ when $E_F = 10E_0$. Since $r_s \sim 1/\sqrt{E_F}$, r_s at any other Fermi energy can be obtained through $r_s(E_F) = \sqrt{10E_0/E_F}$.

In Fig. 10, we plot $\text{Im}\chi_H(\omega + i\delta, \mathbf{q})$ in the charged system, using $E_F = 10E_0$ in Fig. 10(a) and $E_F = 0.1E_0$ in Fig. 10(b). Compared with Fig. 8(a), the only significant difference in the spectral function is in the ABG mode. The ABG mode, which disperses linearly with q in the neutral system, transforms into the plasmon in the charged system, which disperses as $\sqrt{q}$ in 2D. More drastically, we find that the inclusion of the Coulomb interaction leads to dramatic depletion of the spectral weight of the gapless mode, especially in the high-density case of Fig. 10(a). To make the plasmon mode visible in Fig. 10(a), we multiplied $\text{Im}\chi_H(\omega + i\delta, \mathbf{q})$ by a factor of five for $\omega < 2\Delta$. This highlights the significant decoupling of amplitude and phase fluctuations in the charged system and is fully consistent with our analytical treatment. Moreover, our numerical results show that the decoupling is not restricted to only small q but persists to substantially larger $q \gtrsim k_F$.

In the case of Fig. 10(b) where we are in the BEC regime, we also find that the Higgs mode is not affected by the Coulomb interaction. In particular, just as in the neutral superfluid (cf. Fig. 9), there is no peak in $\text{Im}\chi_H(\omega + i\delta, \mathbf{q})$ which can be attributed to the Higgs mode. This agrees with the results of Ref. [33]. Instead, we only have a plasmon peak below the two-particle continuum.

From Fig. 10, we see that the plasmon is much more visible in the Higgs spectral function in the BEC limit compared with the BCS limit, where we artificially multiplied the plasmon spectral weight by a factor of five to make it visible. This difference in visibility between the BEC and BCS limits can also seen in the neutral system (cf. Figs. 8 and 9.) However, the difference is much more stark in the charged system, suggesting that the phase-amplitude mixing at nonzero q grows quickly as we move from the BCS to the BEC limit.
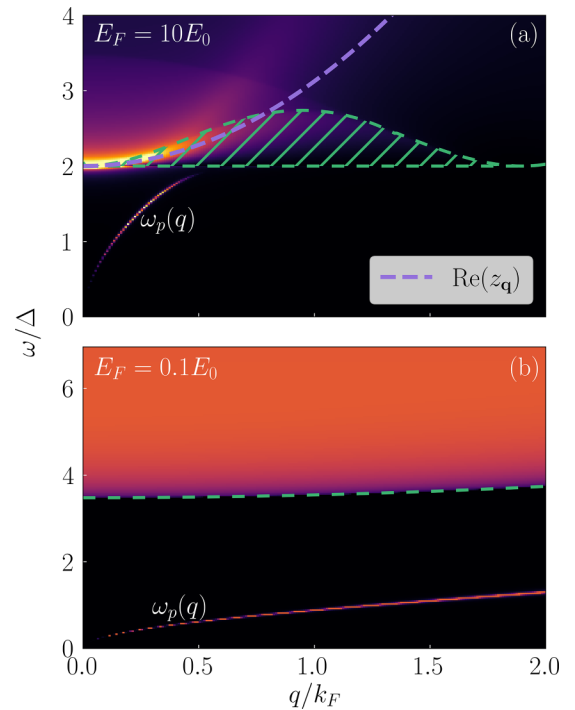

FIG. 10. The spectral function $\text{Im}\chi_H(\omega + i\delta, \mathbf{q})$ in the charged system, for (a) $E_F = 10E_0$ and (b) $E_F = 0.1E_0$, setting $\delta = 10^{-5}\Delta$. As in Fig. 8, the hatched green region in panel (a) corresponds to frequencies between 2Δ and ω_2. Poles with $\text{Re}(z_{\mathbf{q}})$ inside this hatched region lead to peaks in the spectral function. The dashed purple line is the analytical result for the small-q dispersion of the Higgs mode. In panel (b), the dashed green curve delineates the boundary of the two-particle continuum at $\omega_{\min} = 2[\Delta^2 + (|\mu| + q^2/8m)^2]^{1/2}$. The dispersive peak below the two-particle continuum in both panels is the plasmon mode $\omega_p(q)$. In panel (a), we scaled $\text{Im}\chi_H(\omega + i\delta, \mathbf{q})$ by a factor of five for $\omega < 2\Delta$ to enhance visibility of the plasmon mode.

VIII. DISCUSSION

In this work, we obtained the dispersion, damping rate, and residue of the Higgs mode in two dimensions across the BCS-BEC crossover and analyzed under which conditions this mode gives rise to a peak in the imaginary part of the Higgs susceptibility, $\text{Im}\chi_H(\omega + i\delta, \mathbf{q})$, a quantity which is observable using spectroscopic probes.

To detect the Higgs mode, we calculated the Higgs susceptibility $\chi_H(z, \mathbf{q})$ in the upper half plane of complex z and obtained its analytic continuation $\chi_H^{\downarrow}(z, \mathbf{q})$ into the lower half plane. We found that $\chi_H^{\downarrow}(z, \mathbf{q})$ has a pole (the Higgs mode), whose location in the lower half plane is $z_{\mathbf{q}} = 2\Delta + (0.5 - i\beta)(q^2/2m)(\mu/\Delta)$ for $\mu > 0$ and small $\mathbf{q}$. Here, the damping parameter β is given by $\beta = 0.4302$ at $\mu \gg \Delta$ and diverges as $\frac{e}{16}\sqrt{2\Delta/\mu}$ for $\mu \ll \Delta$. Additionally, we calculated the residue $Z_{\mathbf{q}}$ of the pole, finding that $Z_{\mathbf{q}}$ scales linearly with q, and goes to zero at $\mu = 0$ as $(\mu/2\Delta)^{1/4}$. We found that for small q, the Higgs mode gives rise to a peak in the observable $\text{Im}\chi_H(\omega + i\delta, \mathbf{q})$ for any positive value of the dressed chemical potential μ. We then numerically obtained the position of the pole at larger q, finding that the Higgs mode does not give rise to a peak in $\text{Im}\chi_H(\omega + i\delta, \mathbf{q})$ once q crosses some threshold value. For negative μ, we found that the Higgs mode is hidden below a branch cut and does not lead to any peak in $\text{Im}\chi_H(\omega + i\delta, \mathbf{q})$. Lastly, we included the effect of the long-range Coulomb interaction and demonstrated that its inclusion does not affect the Higgs mode, despite the fact that it decouples the phase (density) and amplitude channels.

A final note: in this work we only decoupled our attractive Hubbard interaction in the particle-particle channel, neglecting its effect on the particle-hole channel. This is valid in the high-density or weak-coupling limits, where particle-hole symmetry holds. Away from these limits, renormalization of $\chi_H(z, \mathbf{q})$ in the particle-hole channel from the Hubbard interaction, similar to our treatment of the Coulomb interaction in Sec. VII, is likely necessary to obtain the correct dispersion of the Higgs mode [61].

In summary, our work adds to a growing corpus of theoretical studies of amplitude excitations in superconductors and other systems [24–35] and particularly to the studies of the coupling between collective modes and a continuum of single-particle excitations [62–68]. The generality of the techniques employed here suggests that analytical continuation may be helpful in the study of other physical problems, such as that of plasmon decay inside the particle-hole continuum of strange metals [69].

[1] P. W. Anderson, Coherent excited states in the theory of superconductivity: Gauge invariance and the Meissner effect, Phys. Rev. **110**, 827 (1958).

[2] P. W. Anderson, Plasmons, gauge invariance, and mass, Phys. Rev. **130**, 439 (1963).

[3] P. B. Littlewood and C. M. Varma, Amplitude collective modes in superconductors and their coupling to charge-density waves, Phys. Rev. B **26**, 4883 (1982).

[4] Y. Ohashi and S. Takada, On the plasma oscillation in superconductivity, J. Phys. Soc. Jpn. **67**, 551 (1998).

[5] R. Shimano and N. Tsuji, Higgs mode in superconductors, Annu. Rev. Condens. Matter Phys. **11**, 103 (2020).

[6] R. Sooryakumar and M. V. Klein, Raman Scattering by Superconducting-Gap Excitations and Their Coupling to Charge-Density Waves, Phys. Rev. Lett. **45**, 660 (1980).

[7] R. Sooryakumar and M. V. Klein, Raman scattering from superconducting gap excitations in the presence of a magnetic field, Phys. Rev. B **23**, 3213 (1981).

[8] P. B. Littlewood and C. M. Varma, Gauge-Invariant Theory of the Dynamical Interaction of Charge Density Waves and Superconductivity, Phys. Rev. Lett. **47**, 811 (1981).

[9] T. Cea and L. Benfatto, Nature and Raman signatures of the Higgs amplitude mode in the coexisting superconducting and charge-density-wave state, Phys. Rev. B **90**, 224515 (2014).

[10] R. Matsunaga, N. Tsuji, H. Fujita, A. Sugioka, K. Makise, Y. Uzawa, H. Terai, Z. Wang, H. Aoki, and R. Shimano, Light-induced collective pseudospin precession resonating with Higgs mode in a superconductor, Science **345**, 1145 (2014).

[11] R. Matsunaga, N. Tsuji, K. Makise, H. Terai, H. Aoki, and R. Shimano, Polarization-resolved terahertz third-harmonic generation in a single-crystal superconductor NbN: Dominance of the Higgs mode beyond the BCS approximation, Phys. Rev. B **96**, 020505(R) (2017).

[12] K. Katsumi, N. Tsuji, Y. I. Hamada, R. Matsunaga, J. Schneeloch, R. D. Zhong, G. D. Gu, H. Aoki, Y. Gallais, and R. Shimano, Higgs Mode in the d-Wave Superconductor $Bi_2Sr_2CaCu_2O_{8+x}$ Driven by an Intense Terahertz Pulse, Phys. Rev. Lett. **120**, 117001 (2018).

[13] X. Yang, C. Vaswani, C. Sundahl, M. Mootz, L. Luo, J. Kang, I. Perakis, C. Eom, and J. Wang, Lightwave-driven gapless superconductivity and forbidden quantum beats by terahertz symmetry breaking, Nat. Photonics **13**, 707 (2019).

[14] H. Chu, M.-J. Kim, K. Katsumi, S. Kovalev, R. D. Dawson, L. Schwarz, N. Yoshikawa, G. Kim, D. Putzky, Z. Z. Li et al., Phase-resolved Higgs response in superconducting cuprates, Nat. Commun. **11**, 4165 (2020).

[15] K. Katsumi, Z. Z. Li, H. Raffy, Y. Gallais, and R. Shimano, Superconducting fluctuations probed by the Higgs mode in $Bi_2Sr_2CaCu_2O_{8+x}$ thin films, Phys. Rev. B **102**, 054510 (2020).

[16] R. Grasset, K. Katsumi, P. Massat, H.-H. Wen, X.-H. Chen, Y. Gallais, and R. Shimano, Terahertz pulse-driven collective mode in the nematic superconducting state of $Ba_{1-x}K_xFe_2As_2$, npj Quantum Mater. **7**, 4 (2022).

[17] R. Grasset, Y. Gallais, A. Sacuto, M. Cazayous, S. Mañas Valero, E. Coronado, and M.-A. Méasson, Pressure-Induced Collapse of the Charge Density Wave and Higgs Mode Visibility in $2H$-TaS_2, Phys. Rev. Lett. **122**, 127001 (2019).

[18] M.-A. Méasson, Y. Gallais, M. Cazayous, B. Clair, P. Rodière, L. Cario, and A. Sacuto, Amplitude Higgs mode in the 2H-NbSe₂ superconductor, Phys. Rev. B **89**, 060503(R) (2014).

[19] R. Grasset, T. Cea, Y. Gallais, M. Cazayous, A. Sacuto, L. Cario, L. Benfatto, and M.-A. Méasson, Higgs-mode radiance and charge-density-wave order in 2H-NbSe₂, Phys. Rev. B **97**, 094502 (2018).

[20] M. Endres, T. Fukuhara, D. Pekker, M. Cheneau, P. Schauß, C. Gross, E. Demler, S. Kuhr, and I. Bloch, The "Higgs" amplitude mode at the two-dimensional superfluid/Mott insulator transition, Nature (London) **487**, 454 (2012).

[21] T. Hong, M. Matsumoto, Y. Qiu, W. Chen, T. R. Gentile, S. Watson, F. F. Awwadi, M. M. Turnbull, S. E. Dissanayake, H. Agrawal *et al.*, Higgs amplitude mode in a two-dimensional quantum antiferromagnet near the quantum critical point, Nat. Phys. **13**, 638 (2017).

[22] A. Moor, A. F. Volkov, and K. B. Efetov, Amplitude Higgs Mode and Admittance in Superconductors with a Moving Condensate, Phys. Rev. Lett. **118**, 047001 (2017).

[23] S. Nakamura, K. Katsumi, H. Terai, and R. Shimano, Nonreciprocal Terahertz Second-Harmonic Generation in Superconducting NbN under Supercurrent Injection, Phys. Rev. Lett. **125**, 097004 (2020).

[24] D. Pekker and C. Varma, Amplitude/Higgs modes in condensed matter physics, Annu. Rev. Condens. Matter Phys. **6**, 269 (2015).

[25] D. Podolsky, A. Auerbach, and D. P. Arovas, Visibility of the amplitude (Higgs) mode in condensed matter, Phys. Rev. B **84**, 174522 (2011).

[26] S. Gazit, D. Podolsky, and A. Auerbach, Fate of the Higgs Mode Near Quantum Criticality, Phys. Rev. Lett. **110**, 140401 (2013).

[27] L. Pollet and N. Prokof'ev, Higgs Mode in a Two-Dimensional Superfluid, Phys. Rev. Lett. **109**, 010401 (2012); K. Chen, L. Liu, Y. Deng, L. Pollet, and N. Prokof'ev, Universal Properties of the Higgs Resonance in $(2 + 1)$-Dimensional U(1) Critical Systems, *ibid.* **110**, 170403 (2013).

[28] D. Podolsky and S. Sachdev, Spectral functions of the Higgs mode near two-dimensional quantum critical points, Phys. Rev. B **86**, 054508 (2012).

[29] A. Rançon and N. Dupuis, Higgs amplitude mode in the vicinity of a $(2 + 1)$-dimensional quantum critical point, Phys. Rev. B **89**, 180501(R) (2014); F. Rose, F. Léonard, and N. Dupuis, Higgs amplitude mode in the vicinity of a $(2 + 1)$-dimensional quantum critical point: A nonperturbative renormalization-group approach, *ibid.* **91**, 224501 (2015).

[30] Y. T. Katan and D. Podolsky, Spectral function of the Higgs mode in $4 - \epsilon$ dimensions, Phys. Rev. B **91**, 075132 (2015).

[31] T. Cea, C. Castellani, and L. Benfatto, Nonlinear optical effects and third-harmonic generation in superconductors: Cooper pairs versus Higgs mode contribution, Phys. Rev. B **93**, 180507(R) (2016).

[32] S. Maiti, A. V. Chubukov, and P. J. Hirschfeld, Conservation laws, vertex corrections, and screening in Raman spectroscopy, Phys. Rev. B **96**, 014503 (2017).

[33] T. Cea, C. Castellani, G. Seibold, and L. Benfatto, Nonrelativistic Dynamics of the Amplitude (Higgs) Mode in Superconductors, Phys. Rev. Lett. **115**, 157002 (2015).

[34] M. Puviani, A. Baum, S. Ono, Y. Ando, R. Hackl, and D. Manske, Calculation of an Enhanced A_{1g} Symmetry Mode Induced by Higgs Oscillations in the Raman Spectrum of High-Temperature Cuprate Superconductors, Phys. Rev. Lett. **127**, 197001 (2021); L. Benfatto, C. Castellani, and T. Cea, Comment on "Calculation of an Enhanced A_{1g} Symmetry Mode Induced by Higgs Oscillations in the Raman Spectrum of High-Temperature Cuprate Superconductors," *ibid.* **129**, 199701 (2022); M. Puviani, A. Baum, S. Ono, Y. Ando, R. Hackl, and D. Manske, Puviani *et al.* Reply:, *ibid.* **129**, 199702 (2022).

[35] L. Schwarz and D. Manske, Theory of driven Higgs oscillations and third-harmonic generation in unconventional superconductors, Phys. Rev. B **101**, 184519 (2020).

[36] A. Volkov and S. M. Kogan, Collisionless relaxation of the energy gap in superconductors, Sov. J. Exp. Theor. Phys. **38**, 1018 (1974).

[37] C. Varma, Higgs boson in superconductors, J. Low Temp. Phys. **126**, 901 (2002).

[38] A. Klein, D. L. Maslov, and A. V. Chubukov, Hidden and mirage collective modes in two dimensional Fermi liquids, npj Quantum Mater. **5**, 55 (2020).

[39] A. Behrle, T. Harrison, J. Kombe, K. Gao, M. Link, J.-S. Bernier, C. Kollath, and M. Köhl, Higgs mode in a strongly interacting fermionic superfluid, Nat. Phys. **14**, 781 (2018).

[40] L. Sobirey, H. Biss, N. Luick, M. Bohlen, H. Moritz, and T. Lompe, Observing the Influence of Reduced Dimensionality on Fermionic Superfluids, Phys. Rev. Lett. **129**, 083601 (2022).

[41] V. A. Andrianov and V. N. Popov, Hydrodynamic action and Bose spectrum of superfluid Fermi systems, Theor. Math. Phys. **28**, 829 (1976).

[42] See Supplemental Material at http://link.aps.org/supplemental/10.1103/PhysRevB.107.134519 for details.

[43] H. Kurkjian, S. N. Klimin, J. Tempere, and Y. Castin, Pair-Breaking Collective Branch in BCS Superconductors and Superfluid Fermi Gases, Phys. Rev. Lett. **122**, 093403 (2019).

[44] M. Randeria, J.-M. Duan, and L.-Y. Shieh, Bound States, Cooper Pairing, and Bose Condensation in Two Dimensions, Phys. Rev. Lett. **62**, 981 (1989).

[45] J. R. Engelbrecht, M. Randeria, and C. A. R. Sáde Melo, BCS to Bose crossover: Broken-symmetry state, Phys. Rev. B **55**, 15153 (1997).

[46] R. B. Diener, R. Sensarma, and M. Randeria, Quantum fluctuations in the superfluid state of the BCS-BEC crossover, Phys. Rev. A **77**, 023626 (2008).

[47] D. Pimenov and A. V. Chubukov, Quantum phase transition in a clean superconductor with repulsive dynamical interaction, npj Quantum Mater. **7**, 45 (2022).

[48] R. Combescot, M. Y. Kagan, and S. Stringari, Collective mode of homogeneous superfluid Fermi gases in the BEC-BCS crossover, Phys. Rev. A **74**, 042717 (2006).

[49] A. V. Chubukov, I. Eremin, and D. V. Efremov, Superconductivity versus bound-state formation in a two-band superconductor with small Fermi energy: Applications to Fe pnictides/chalcogenides and doped SrTiO₃, Phys. Rev. B **93**, 174516 (2016).

[50] DLMF, NIST Digital Library of Mathematical Functions, http://dlmf.nist.gov/, Release 1.1.8 of 2022-12-15, edited by W. J. Olver *et al.* (2022).

[51] H. Zhao, X. Gao, W. Liang, P. Zou, and F. Yuan, Dynamical structure factors of a two-dimensional Fermi superfluid within random phase approximation, New J. Phys. **22**, 093012 (2020).

[52] $\omega_{\mathbf{q}}$ and $\gamma_{\mathbf{q}}$ also change with the threshold, but continue to fit the analytical expressions relatively well regardless of the precise threshold used.

[53] B. I. Epureanu and H. S. Greenside, Fractal basins of attraction associated with a damped Newton's method, SIAM Rev. **40**, 102 (1998).

[54] Y. Castin and H. Kurkjian, Collective excitation branch in the continuum of pair-condensed fermi gases: Analytical study and scaling laws, arXiv:1907.12238; Branche d'excitation collective du continuum dans les gaz de fermions condensés par paires: étude analytique et lois d'échelle, C. R. Phys. **21**, 253 (2020).

[55] D. Mozyrsky and A. V. Chubukov, Dynamic properties of superconductors: Anderson-Bogoliubov mode and Berry phase in the BCS and BEC regimes, Phys. Rev. B **99**, 174510 (2019).

[56] P. Morel and P. W. Anderson, Calculation of the superconducting state parameters with retarded electron-phonon interaction, Phys. Rev. **125**, 1263 (1962).

[57] M. Grabowski and L. J. Sham, Superconductivity from non-phonon interactions, Phys. Rev. B **29**, 6132 (1984).

[58] D. Phan and A. V. Chubukov, Effect of repulsion on superconductivity at low density, Phys. Rev. B **105**, 064518 (2022).

[59] W. Kohn and J. M. Luttinger, New Mechanism for Superconductivity, Phys. Rev. Lett. **15**, 524 (1965).

[60] S. Maiti and A. V. Chubukov, *Superconductivity from Repulsive Interaction*, AIP Conf. Proc. No. 1550 (American Institute of Physics, 2013), pp. 3–73..

[61] L. Benfatto, A. Toschi, S. Caprara, and C. Castellani, Coherence length in superconductors from weak to strong coupling, Phys. Rev. B **66**, 054515 (2002).

[62] S. N. Klimin, J. Tempere, and H. Kurkjian, Phononic collective excitations in superfluid Fermi gases at nonzero temperatures, Phys. Rev. A **100**, 063634 (2019).

[63] S. Klimin, H. Kurkjian, and J. Tempere, Leggett collective excitations in a two-band Fermi superfluid at finite temperatures, New J. Phys. **21**, 113043 (2019).

[64] L.-P. Lumbeeck, J. Tempere, and S. Klimin, Dispersion and damping of phononic excitations in Fermi superfluid gases in 2D, Condens. Matter **5**, 13 (2020).

[65] H. Kurkjian, J. Tempere, and S. Klimin, Linear response of a superfluid Fermi gas inside its pair-breaking continuum, Sci. Rep. **10**, 11591 (2020).

[66] S. N. Klimin, J. Tempere, and H. Kurkjian, Collective excitations of superfluid Fermi gases near the transition temperature, Phys. Rev. A **103**, 043336 (2021).

[67] T. Repplinger, S. Klimin, M. Gélédan, J. Tempere, and H. Kurkjian, Plasmons in three-dimensional superconductors, Phys. Rev. B **107**, 014504 (2023).

[68] S. Klimin, J. Tempere, T. Repplinger, and H. Kurkjian, Collective excitations of a charged fermi superfluid in the BCS-BEC crossover, arXiv:2208.09757.

[69] X. Wang and D. Chowdhury, Collective density fluctuations of strange metals with critical Fermi surfaces, Phys. Rev. B **107**, 125157 (2023).